

Long Distance GNSS-Denied Visual Inertial Navigation for Autonomous Fixed Wing Unmanned Air Vehicles: $\text{SO}(3)$ Manifold Filter based on Virtual Vision Sensor

Eduardo Gallo^{*†} and Antonio Barrientos^{‡§}

March 2023

Abstract

This article proposes a visual inertial navigation algorithm intended to diminish the horizontal position drift experienced by autonomous fixed wing UAVs (Unmanned Air Vehicles) in the absence of GNSS (Global Navigation Satellite System) signals. In addition to accelerometers, gyroscopes, and magnetometers, the proposed navigation filter relies on the accurate incremental displacement outputs generated by a VO (Visual Odometry) system, denoted here as a Virtual Vision Sensor or VVS, which relies on images of the Earth surface taken by an onboard camera and is itself assisted by the filter inertial estimations. Although not a full replacement for a GNSS receiver since its position observations are relative instead of absolute, the proposed system enables major reductions in the GNSS-Denied attitude and position estimation errors. In order to minimize the accumulation of errors in the absence of absolute observations, the filter is implemented in the manifold of rigid body rotations or $\text{SO}(3)$. Stochastic high fidelity simulations of two representative scenarios involving the loss of GNSS signals are employed to evaluate the results. The authors release the C++ implementation of both the visual inertial navigation filter and the high fidelity simulation as open-source software [1].

Keywords: GNSS-Denied, visual inertial navigation, autonomous navigation, EKF, autonomy, VIO

Mathematical Notation

Any variable with a hat accent $\langle \hat{\cdot} \rangle$ refers to its (inertial) estimated value, with a circular accent $\langle \circ \cdot \rangle$ to its (visual) estimated value, with a tilde $\langle \tilde{\cdot} \rangle$ to its measured value, and with a dot $\langle \cdot \dot{\cdot} \rangle$ to its time derivative. In the case of vectors, which are displayed in bold (e.g., \mathbf{x}), other employed symbols include the wide hat $\langle \widehat{\cdot} \rangle$, which refers to the skew-symmetric form, and the double vertical bars $\langle \|\cdot\| \rangle$, which refer to the norm. In the case of scalars, the vertical bars $\langle |\cdot| \rangle$ refer to the absolute value. When employing quaternions, which are also displayed in bold (e.g., \mathbf{q}), the asterisk superindex $\langle \cdot^* \rangle$ refers to the conjugate, their concatenation and multiplication are represented by \circ and \otimes respectively, and \oplus and \ominus refer to the plus and minus operators.

This article makes use of the space of rigid body rotations, and hence relies on the Lie algebra of the special orthogonal group of \mathbb{R}^3 , known as $\text{SO}(3)$, in particular what refers to the group actions, concatenations, perturbations, and Jacobians, as well its tangent spaces, the rotation vector \mathbf{r} and the angular velocity $\boldsymbol{\omega}$. [2, 3, 4] are recommended as references.

^{*}Contact: e.gallo@alumnos.upm.es, edugallo@yahoo.com, <https://orcid.org/0000-0002-7397-0425>

[†]Affiliation: Centro de Automática y Robótica, Universidad Politécnica de Madrid - Consejo Superior de Investigaciones Científicas. Centre for Automation and Robotics, Polytechnic University of Madrid.

[‡]Contact: antonio.barrientos@upm.es, <https://orcid.org/0000-0003-1691-3907>

[§]Affiliation: Centro de Automática y Robótica, Universidad Politécnica de Madrid - Consejo Superior de Investigaciones Científicas. Centre for Automation and Robotics, Polytechnic University of Madrid.

Four different reference frames are employed in this article: the ECEF frame F_E ¹, the NED frame F_N ², the body frame F_B ³, and the inertial frame F_I ⁴. Superindexes are employed over vectors to specify the reference frame in which they are viewed (e.g., \mathbf{v}^N refers to ground velocity viewed in NED, while \mathbf{v}^B is the same vector but viewed in body). Subindexes may be employed to clarify the meaning of the variable or vector, such as in \mathbf{v}_{TAS} for air velocity instead of the ground velocity \mathbf{v} , in which case the subindex is either an acronym or its meaning is clearly explained when first introduced. Subindexes may also refer to a given component of a vector, e.g. v_2^N refers to the second component of \mathbf{v}^N . In addition, where two reference frames appear as subindexes to a vector, it means that the vector goes from the first frame to the second. For example, $\boldsymbol{\omega}_{NB}^B$ refers to the angular velocity from NED to body viewed in body.

1 Introduction and Outline

The main objective of this article is to develop a navigation system capable of diminishing the position drift inherent to the flight in GNSS (Global Navigation Satellite System) Denied conditions of autonomous fixed wing aircraft, so in case GNSS signals become unavailable during flight, they have a higher probability of reaching the vicinity of a distant recovery point, from where they can be landed by remote control.

The proposed method combines two different navigation systems (inertial and visual) in such a way that both simultaneously assist and control each other. The inertial attitude and altitude estimations are employed to bound their visual counterparts, resulting in major improvements in the accuracy of the visual horizontal position estimations; these in turn are fed back to the inertial filter in the form of incremental displacement observations, diminishing its estimation errors and partially replacing the GNSS receiver. The resulting horizontal position estimation errors are just a small fraction of what can be obtained by inertial or visual algorithms operating independently. In contrast with most visual inertial methods found in the literature, which focus on the short term GNSS-Denied navigation of ground vehicles, robots, and multirotors, the proposed algorithms are primarily intended for the long distance GNSS-Denied navigation of autonomous fixed wing aircraft.

Section 2 describes the article novelty and main applications. The proposed architecture when combining the inertial and visual navigation algorithms is discussed in section 3. Section 4 introduces the VVS (Virtual Vision Sensor), which is just a different name for an advanced visual odometry pipeline assisted by the inertial outputs. The VVS outputs containing the accurate incremental displacement visual estimations are then supplied to a navigation filter implemented in the tangent space to the $\mathbb{SO}(3)$ aircraft attitude; section 5 contains a detailed explanation of the filter equations. The operation of the fully integrated closed loop visual inertial navigation system is described in section 6.

Section 7 introduces the stochastic high fidelity simulation employed to evaluate the navigation results by means of Monte Carlo executions of two scenarios representative of the challenges of GNSS-Denied navigation. The results obtained when applying the proposed algorithms to these two GNSS-Denied scenarios are described in section 8, comparing them with those achieved by standalone inertial and visual systems. Last, the results are summarized for convenience in section 9, while section 10 provides a short conclusion.

The article concludes with two appendices that are better placed outside the main flow of the document. Appendix A contains an introduction to GNSS-Denied navigation and its challenges, together with reviews of the state-of-the-art in two of the most promising routes to diminish its negative effects, such as *visual odometry (VO)* and *visual inertial odometry (VIO)*. Appendix B describes the obtainment of various Jacobians required for the proposed

¹The ECEF frame is centered at the Earth center of mass, with \mathbf{i}_3^E pointing towards the geodetic North along the Earth rotation axis, \mathbf{i}_1^E contained in both the Equator and zero longitude planes, and \mathbf{i}_2^E orthogonal to \mathbf{i}_1^E and \mathbf{i}_3^E forming a right handed system.

²The NED frame is centered at the aircraft center of mass, with axes aligned with the geodetic North, East, and Down directions.

³The body frame is centered at the aircraft center of mass, with \mathbf{i}_1^B contained in the plane of symmetry of the aircraft pointing forward along a fixed direction, \mathbf{i}_3^B contained in the plane of symmetry of the aircraft, normal to \mathbf{i}_1^B and pointing downward, and \mathbf{i}_2^B orthogonal to both in such a way that they form a right hand system.

⁴The inertial frame is centered at the Earth center of mass and its axes do not rotate with respect to any stars other than the Sun.

navigation filter in section 5.

2 Novelty and Application

The proposed approach combines two different navigation systems (inertial and visual) in such a way that both simultaneously assist and control each other, resulting in a virtuous (positive) feed back loop with major improvements in horizontal position estimation accuracy compared with either system by itself.

When compared to the state-of-the-art discussed in appendix A, the proposed system combines the high accuracy representative of tightly coupled smoothers with the lack of complexity and reduced computing requirements of filters and loosely coupled approaches. The existence of two independent solutions (inertial and visual) hints to a loosely coupled approach, but in fact the proposed solution shares most traits with tightly coupled pipelines. First, no information is discarded because the two solutions are not independent, as each simultaneously feeds and is fed by the other. The visual estimations depend on the inertial attitude and altitude outputs, while the inertial filter uses the visual incremental displacement estimations as observations. Unlike loosely coupled solutions, the visual estimations for attitude and altitude are not allowed to deviate from the inertial ones above a certain threshold, so they do not drift. Additionally, the two estimations are never fused together, as the inertial solution constitutes the final output, while the sole role of the visual outputs is to act as the previously mentioned incremental sensor. The proposed solution contains both a filter within the inertial system as well as a keyframe based sliding window smoother within the visual one, obtaining the best properties of both categories.

The **VIO** solutions listed in appendix A are quite generic with respect to the platforms on which they are mounted, with most applications focused on ground vehicles, indoor robots, and multirotors, as well as with respect to the employed sensors, which are usually restricted to the Inertial Measurement Unit (**IMU**) and one or more cameras. This article focuses on a specific case (long distance **GNSS**-Denied turbulent flight of fixed wing autonomous aircraft), and as such it is more restricted in its application, but can also take advantage of the extra sensors already present onboard these platforms (magnetometers, barometer), is better suited to the particular motion of these types of vehicles (forward motion is orders of magnitude faster than those in the lateral and vertical directions), and acts as a solution to **GNSS**-Denied environments of a different nature than those experienced by those platforms (it can be assumed that **GNSS** signals are present at the beginning of the flight, and if they disappear, the reason is likely to be technical error or intentional action, so the vehicle needs to be capable of flying for long periods of time in **GNSS**-Denied conditions).

The proposed system however does not constitute a full **GNSS** replacement as it relies on incremental instead of absolute position observations and hence can only reduce the position drift but not eliminate it. Additionally, it imposes certain restrictions on its usage, such as the need for day light, lack of cloud cover below the aircraft, and impossibility to navigate over large bodies of water.

This article proves that inertial and visual navigation systems of a **UAV** (Unmanned Air Vehicle) can be combined in such a way that the resulting long term **GNSS**-Denied horizontal position drift is significantly smaller than what can be obtained by either system individually. In the case that **GNSS** signals become unavailable in mid flight, **GNSS**-Denied navigation is required for the platform to complete its mission or return to base without the absolute position and ground velocity observations provided by **GNSS** receivers. As shown in the following sections, the proposed system can significantly increase the possibilities of the **UAV** safely reaching the vicinity of the intended recovery location, from where it can be landed by remote control.

3 Proposed Visual Inertial Navigation Architecture

The navigation system processes the measurements of the various onboard sensors ($\tilde{\mathbf{x}} = \mathbf{x}_{\text{SENSED}}$) and generates the estimated state ($\hat{\mathbf{x}} = \mathbf{x}_{\text{EST}}$) required by the guidance and control systems, which contains the best possible estimations of the true aircraft state $\mathbf{x} = \mathbf{x}_{\text{TRUTH}}$. Note that in this article the images \mathbf{I} are considered part of

the sensed states $\tilde{\mathbf{x}} = \mathbf{x}_{\text{SENSED}}$ as the camera is treated as an additional sensor. Hardware and computing power limitations often require the camera and visual navigation algorithms to operate at a lower frequency than those of the sensors and inertial algorithms; table 1 includes the operating frequencies employed in this article.

Discrete Time	Frequency	Period	Variables	Systems
$t_t = t \cdot \Delta t_{\text{TRUTH}}$	500 Hz	0.002 s	$\mathbf{x} = \mathbf{x}_{\text{TRUTH}}$	Flight physics
$t_s = s \cdot \Delta t_{\text{SENSED}}$	100 Hz	0.01 s	$\tilde{\mathbf{x}} = \mathbf{x}_{\text{SENSED}}$	Sensors
$t_n = n \cdot \Delta t_{\text{EST}}$	100 Hz	0.01 s	$\hat{\mathbf{x}} = \mathbf{x}_{\text{EST}}$	Inertial navigation
$t_c = c \cdot \Delta t_{\text{CNTR}}$	50 Hz	0.02 s	$\delta_{\text{TARGET}}, \delta_{\text{CNTR}}$	Guidance & control
$t_i = i \cdot \Delta t_{\text{IMG}}$	10 Hz	0.1 s	$\dot{\mathbf{x}} = \mathbf{x}_{\text{IMG}}$	Visual navigation & camera
$t_g = g \cdot \Delta t_{\text{GNSS}}$	1 Hz	1 s		GNSS receiver

Table 1: Working frequencies of the different systems

A previous article by the same authors, [5], shows that by freezing the atmospheric and wind estimations at the time the GNSS signals are lost, it is possible to develop an EKF based Inertial Navigation System (INS) for fixed wing aircraft that results in bounded (no drift) estimations for attitude, altitude, and ground velocity⁵, as well as an unavoidable drift in horizontal position caused by integrating the ground velocity without absolute observations. Figure 1 graphically depicts that the INS inputs include all sensor measurements with the exception of the camera images \mathbf{I} .

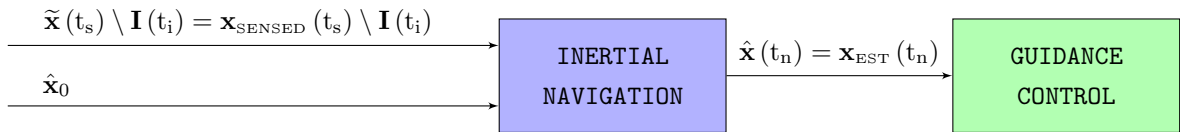


Figure 1: INS flow diagram

A second article, [6], focuses on visual navigation (that which exclusively relies on the images generated by an onboard camera). Based on the open-source Semi Direct Visual Odometry (SDVO) pipeline [7, 8] introduced in appendix A, it results in a slow but unrestricted error growth or drift in body attitude, altitude, and horizontal position estimations. As excessive attitude errors may create instability issues if they exceed certain thresholds past which the control system is unable to operate as intended, [6] implements the Visual Navigation System (VNS) in an open loop configuration (figure 2), in which the guidance and control systems continue to rely on the inertial (INS) estimations $\hat{\mathbf{x}} = \mathbf{x}_{\text{EST}}$, while the visual states $\dot{\mathbf{x}} = \mathbf{x}_{\text{IMG}}$ are only employed for VNS evaluation.

The strategy to fuse the inertial and visual navigation systems is based on their performances as standalone systems, as summarized in table 2. Inertial systems are clearly superior to visual ones in four out of the six degrees of freedom (attitude and altitude), since their GNSS-Denied estimations are bounded and do not drift. In the case of horizontal position, both systems drift and are hence inappropriate for long term GNSS-Denied navigation, but for different reasons; while the INS drift is the result of integrating the bounded ground velocity estimations without absolute position observations, that of the VNS originates on the slow but continuous accumulation of estimation errors between consecutive images.

It is also worth noting that inertial estimations are significantly noisier than visual ones, so the latter, although worse on an absolute basis, are often more accurate when evaluating the estimations incrementally, this is, from one image to the next or even for the time interval corresponding to a few images.

The fusion between the inertial and visual navigation systems is accomplished in two phases. In the first, the inertial pitch, bank, and altitude bounded estimations are supplied as targets to the VNS, which is now denoted as the Inertially Assisted VNS or IA-VNS, so the visual pitch, bank, and vertical position estimations do not

⁵A bounded attitude estimation ensures that the aircraft can remain aloft in GNSS-Denied conditions for as long as there is fuel available. The altitude estimation error depends on the change in atmospheric pressure offset from its value at the time the GNSS signals are lost, which is bounded by atmospheric physics. The ground velocity estimation error depends on the change in wind velocity from its value at the time the GNSS signals are lost, which is also bounded by atmospheric physics.

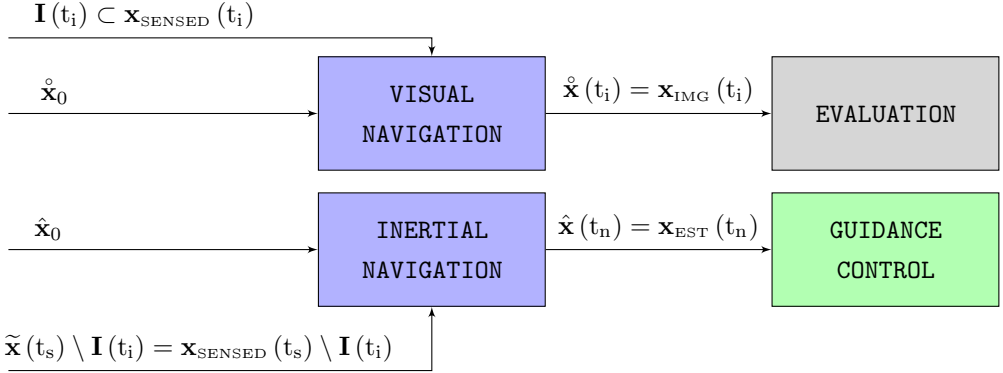


Figure 2: VNS flow diagram

deviate in excess from their inertial counterparts. This process, described in detail in [6], relies on the addition of priors to the nonlinear pose optimizations within **SVO**, and does not only result in significantly improved visual estimations for these variables, but more importantly, it also improves the fit between the terrain map built by **SVO** and the features present in the images, resulting in a major reduction of the horizontal position estimation errors when compared with those achieved by the standalone **INS** or **VNS**. Because the drift is reduced but not fully eliminated, the **IA-VNS** within [6] is also implemented in the open loop configuration depicted in figure 3, in which the visual outputs are only employed for evaluation purposes.

GNSS-Denied	Inertial (INS)	Visual (VNS)
Attitude	Bounded by sensor quality	Drifts
	Yaw worse than pitch and bank	Yaw better than pitch and bank
Vertical	Bounded by atmospheric physics	Drifts
Horizontal	Drifts	Drifts

Table 2: Summary of inertial and visual standalone navigation systems

The **IA-VNS** qualitative properties are the same as those of the **VNS** listed in table 2, but quantitatively the drift is significantly lower for five degrees of freedom (yaw accuracy does not change, as discussed in [6]). Of particular interest is the fact that the horizontal position estimations from one image to the next, this is, the incremental displacement observations (equivalent to ground velocity observations), are also even more accurate for the **IA-VNS** than the already accurate **VNS** ones, which constitutes the basis of the second phase.

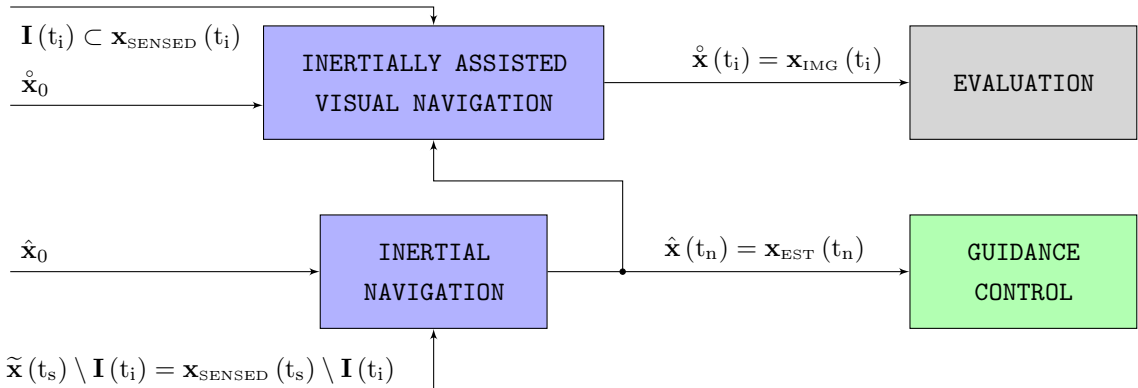


Figure 3: IA-VNS flow diagram

This article proposes an inertial navigation filter implemented on the manifold of rigid body rotations or $\mathbb{SO}(3)$ [2, 4], which in the absence of **GNSS** signals takes advantage of the $\dot{\mathbf{x}} = \mathbf{x}_{\text{IMG}}$ **IA-VNS** incremental displacement outputs as if they were the observations generated by an additional sensor denoted as the Virtual Vision Sensor or **VVS** (section 4). In the proposed **EKF** (section 5), the inertial navigation filter relies on the observations provided by the onboard accelerometers, gyroscopes, and magnetometers, combined with those of the **GNSS** receiver when

signals are available, or those of the VVS when they are not.

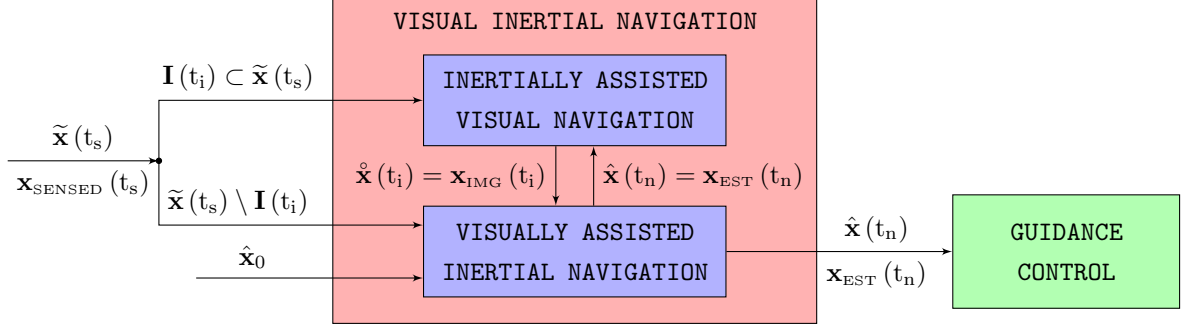


Figure 4: VINS flow diagram

The fully integrated Visual Inertial Navigation System or VINS, graphically depicted in figure 4, discards the original standalone INS and fuses the inertial and visual algorithms so they simultaneously feed and are fed by each other. This creates a positive feed back loop, in which the IA-VNS or VVS horizontal position estimation improvements are successfully transferred to the inertial system (now denoted as the Visually Assisted INS or VA-INS), generating significant reductions in its attitude estimation errors, which in turn generate a second round of major improvements in horizontal position estimation accuracy, as discussed in section 8.

4 Virtual Vision Sensor

The *virtual vision sensor* (VVS) constitutes an alternative denomination for the incremental displacement outputs obtained by the IA-VNS [6]. Although the IA-VNS horizontal position estimations are significantly more accurate than those of the standalone VNS (section 8), they still drift with time due to the absence of absolute observations. When evaluated on an incremental basis, this is, from one image to the next, the IA-VNS incremental displacement estimations are however quite accurate. This section shows how to convert these incremental estimations into measurements for the geodetic coordinates ($\tilde{\mathbf{T}}^{E,GDT}$) and the ground velocity viewed in NED ($\tilde{\mathbf{v}}^N$), so the VVS can smoothly replace the GNSS receiver within the navigation filter (section 5) in the absence of GNSS signals.

Their obtainment relies on the current visual state $\dot{\mathbf{x}}(t_i) = \mathbf{x}_{IMG}(t_i) = \dot{\mathbf{x}}_i$ generated by the visual system (IA-VNS), the one obtained with the previous frame $\dot{\mathbf{x}}(t_{i-1}) = \mathbf{x}_{IMG}(t_{i-1}) = \dot{\mathbf{x}}_{i-1}$, as well as the inertial state $\dot{\mathbf{x}}(t_{n-\delta t}) = \mathbf{x}_{EST}(t_{n-\delta t}) = \dot{\mathbf{x}}_{n-\delta t}$ corresponding to the previous image generated by the inertial system (VA-INS). Note that as $t = t_i = i \cdot \Delta t_{IMG} = t_n = n \cdot \Delta t_{EST}$, the relationship between i and n is as follows, where $\delta t = 10$ is the number of inertial executions for every image being processed (table 1):

$$n = i \cdot \frac{\Delta t_{IMG}}{\Delta t_{EST}} = i \cdot \delta t \quad (1)$$

To obtain the VVS velocity ($\tilde{\mathbf{v}}^N$) observations, it is necessary to first compute the geodetic coordinates (longitude λ , latitude φ , altitude h) derivative as the time difference between their values corresponding to the last two images (2), followed by their transformation into $\tilde{\mathbf{v}}^N$ per (3)⁶. Note that $\tilde{\mathbf{v}}^N$ is very noisy given how it is obtained.

$$\dot{\mathbf{T}}_i^{E,GDT} = \begin{bmatrix} \dot{\lambda}_i & \dot{\varphi}_i & \dot{h}_i \end{bmatrix}^T = \frac{\dot{\mathbf{T}}_i^{E,GDT} - \dot{\mathbf{T}}_{i-1}^{E,GDT}}{\Delta t_{IMG}} \quad (2)$$

$$\tilde{\mathbf{v}}_n^N = \begin{bmatrix} \left[M(\tilde{\varphi}_{n-\delta t}) + \tilde{h}_{n-\delta t} \right] \dot{\varphi}_i & \left[N(\tilde{\varphi}_{n-\delta t}) + \tilde{h}_{n-\delta t} \right] \cos \tilde{\varphi}_{n-\delta t} \dot{\lambda}_i & -\dot{h}_i \end{bmatrix}^T \quad (3)$$

With respect to the VVS geodetic coordinates, the sensed longitude $\tilde{\lambda}$ and latitude $\tilde{\varphi}$ can be obtained per (5) and (6) based on incrementing the previous inertial estimations (those corresponding to the time of the previous VVS reading) with their visually obtained derivatives. To avoid drift, the geometric altitude \tilde{h} is estimated based on

⁶M and N represent the WGS84 radii of curvature of meridian and prime vertical, respectively.

the barometer observations assuming that the atmospheric pressure offset remains frozen from the time the **GNSS** signals are lost⁷.

$$\tilde{\mathbf{T}}_n^{E,GDT} = \begin{bmatrix} \tilde{\lambda}_n & \tilde{\varphi}_n & \tilde{h}_n \end{bmatrix}^T \quad (4)$$

$$\tilde{\lambda}_n = \hat{\lambda}_{n-\delta t} + \dot{\lambda}_i \Delta t_{IMG} \quad (5)$$

$$\tilde{\varphi}_n = \hat{\varphi}_{n-\delta t} + \dot{\varphi}_i \Delta t_{IMG} \quad (6)$$

With respect to the covariances, the authors have assigned the **VVS** an ad-hoc position standard deviation one order of magnitude lower than that employed for the **GNSS** receiver so the navigation filter (section 5) closely tracks the position observations provided by the **VVS**⁸. Given the noisy nature of the virtual velocity observations, the authors have preferred to employ a dynamic evaluation for the velocity standard deviation, which coincides with the absolute value (for each of the three dimensions) of the difference between each new velocity observation and the running average of the last twenty readings (equivalent to the last 2 s).

5 Proposed Navigation Filter

As graphically depicted in figure 4, the navigation filter inside the Visually Assisted **INS** or **VA-INS** estimates the aircraft pose $\hat{\mathbf{x}} = \mathbf{x}_{EST}$ based on the observations provided by the onboard sensors $\tilde{\mathbf{x}} \setminus \mathbf{I} = \mathbf{x}_{SENSED} \setminus \mathbf{I}$ complemented if necessary (in the absence of **GNSS** signals) by the visual observations $\dot{\mathbf{x}} = \mathbf{x}_{IMG}$ provided by the **VVS**. Implemented as an **EKF**, the objective of the navigation filter is the estimation of the aircraft attitude or rotation between the **NED** and body frames represented by its unit quaternion \mathbf{q}_{NB} [2, 3] together with the aircraft position represented by its geodetic coordinates $\mathbf{T}^{E,GDT}$, although it also estimates the aircraft angular velocity ω_{NB}^B (from **NED** to body viewed in body), the ground velocity \mathbf{v}^N viewed in **NED**, the specific force \mathbf{f}_{IB}^B or non gravitational acceleration from the inertial to the body frame viewed in body, the full gyroscope, accelerometer, and magnetometer errors (\mathbf{E}_{GYR} , \mathbf{E}_{ACC} , \mathbf{E}_{MAG})⁹, and the difference \mathbf{B}_{DEV}^N between the Earth magnetic field provided by the onboard model \mathbf{B}_{MOD}^N and the real one \mathbf{B}_{REAL}^N .

$$\mathbf{x}(t) = [\mathbf{q}_{NB} \ \omega_{NB}^B \ \mathbf{T}^{E,GDT} \ \mathbf{v}^N \ \mathbf{f}_{IB}^B \ \mathbf{E}_{GYR} \ \mathbf{E}_{ACC} \ \mathbf{E}_{MAG} \ \mathbf{B}_{DEV}^N]^T \quad (7)$$

As the body attitude \mathbf{q}_{NB} belongs to the non Euclidean *special orthogonal group* or $\mathbb{SO}(3)$, the classical **EKF** scheme [2, 10], which relies on linear algebra, shall be avoided in favor of an alternative formulation to ensure that the estimated attitude never deviates from its $\mathbb{SO}(3)$ manifold [11]¹⁰. The use of Lie theory, with its manifolds and tangent spaces, enables the construction of rigorous calculus techniques to handle uncertainties, derivatives, and integrals of non Euclidean elements with precision and ease [4].

The most rigorous and precise way to adapt the **EKF** scheme to the presence of non Euclidean elements such as rigid body rotations (\mathbf{q}_{NB}) is to exclude the rotation element $\mathcal{R} \in \mathbb{SO}(3)$ from the state system, replacing the unit quaternion \mathbf{q}_{NB} by a local (body) tangent space perturbation represented by the rotation vector $\Delta \mathbf{r}_{NB}^B \in \mathbb{R}^3$ [2, 4]. Note that the state vector also contains the velocity of \mathcal{R} as it moves along its manifold (its angular velocity), contained in the local or body tangent space. Each filter step now consists on estimating the rotation element $\hat{\mathcal{R}}_n = \hat{\mathcal{R}}(t_n) \in \mathbb{SO}(3)$, the state vector $\hat{\mathbf{x}}_n = \hat{\mathbf{x}}(t_n) = [\Delta \mathbf{r}_{NBn}^B \ \hat{\omega}_{NBn}^B \ \hat{\mathbf{z}}_n]^T \in \mathbb{R}^{27}$, and its covariance $\mathbf{P}_n = \mathbf{P}(t_n) \in \mathbb{R}^{27 \times 27}$, based on their values at $t_{n-1} = (n-1) \Delta t$.

$$\mathcal{R}(t) = \mathbf{q}_{NB} \in \mathbb{SO}(3)(t) \quad (8)$$

⁷The interested reader should refer to [5] for a detailed explanation on how to estimate the geometric altitude without **GNSS** signals.

⁸The **GNSS** receiver position covariance is higher so the navigation filter slowly corrects the position estimations obtained from integrating the state equations instead of closely adhering to the noisy **GNSS** position measurements.

⁹ \mathbf{E}_{GYR} , \mathbf{E}_{ACC} , and \mathbf{E}_{MAG} include all gyroscope, accelerometer, and magnetometer error sources except system noise, as explained in [9].

¹⁰As \mathbf{q}_{NB} is not Euclidean, the direct application of the classical **EKF** scheme would result in the need to continuously reproject (normalize) the estimated quaternions back to the manifold as otherwise the estimated states would not comply with the constraints (orthogonality and handedness in the case of rigid body rotations). The repeated deviations and reprojections from and to the manifold may result in a significant degradation in the estimation accuracy [2, 4].

$$\begin{aligned}\mathbf{x}(t) &= [\Delta \mathbf{r}_{\text{NB}}^{\text{B}} \ \boldsymbol{\omega}_{\text{NB}}^{\text{B}} \ \mathbf{z}]^{\text{T}} = [\Delta \mathbf{r}_{\text{NB}}^{\text{B}} \ \mathbf{p}]^{\text{T}} \\ &= [\Delta \mathbf{r}_{\text{NB}}^{\text{B}} \ \boldsymbol{\omega}_{\text{NB}}^{\text{B}} \ \mathbf{T}^{\text{E,GDT}} \ \mathbf{v}^{\text{N}} \ \mathbf{f}_{\text{IB}}^{\text{B}} \ \mathbf{E}_{\text{GYR}} \ \mathbf{E}_{\text{ACC}} \ \mathbf{E}_{\text{MAG}} \ \mathbf{B}_{\text{DEV}}^{\text{N}}]^{\text{T}} \in \mathbb{R}^{27}(t)\end{aligned}\quad (9)$$

The observations \mathbf{y}_n are provided by the gyroscopes, which measure the angular velocity $\tilde{\boldsymbol{\omega}}_{\text{IB}}^{\text{B}}$ from the inertial frame to the body frame viewed in body, the accelerometers that provide the specific force $\tilde{\mathbf{f}}_{\text{IB}}^{\text{B}}$ or non gravitational acceleration from the inertial to the body frame viewed in body, the magnetometers that measure the magnetic field $\tilde{\mathbf{B}}^{\text{B}}$ in the body frame, and either the GNSS receiver or the VVS (section 4) that provide the absolute position (geodetic coordinates) and NED velocity observations $(\tilde{\mathbf{T}}^{\text{E,GDT}}, \tilde{\mathbf{v}}^{\text{N}})$. Note that the measurements are provided at different frequencies, as listed in table 1; most are available every $\Delta t_{\text{SENSED}} = 0.01$ s, but the ground velocity and position measurements are generated every $\Delta t_{\text{GNSS}} = 1$ s if provided by the GNSS receiver or every $\Delta t_{\text{IMG}} = 0.1$ s when the GNSS signals are not available and the readings are instead supplied by the VVS.

$$\mathbf{y}_n = \left[\tilde{\boldsymbol{\omega}}_{\text{IB}}^{\text{B}} \ \tilde{\mathbf{f}}_{\text{IB}}^{\text{B}} \ \tilde{\mathbf{B}}^{\text{B}} \ \tilde{\mathbf{T}}^{\text{E,GDT}} \ \tilde{\mathbf{v}}^{\text{N}} \right]^{\text{T}} \in \mathbb{R}_n^{15} \quad (10)$$

The variation with time of the state variables (11) comprises a continuous time nonlinear state system composed by three exact equations (with no simplifications) containing the rotational motion time derivative (12) [2, 4], the kinematics of the geodetic coordinates (13)¹¹, as well as the aircraft velocity dynamics (14) [5], together with six other differential equations (15) in which the filter does not posses any knowledge about the time derivatives of the state variables, which are set to zero. Note that in expression (14), $\mathbf{g}_*(\cdot)$ represents the $\mathbb{SO}(3)$ group rotation action, \oplus constitutes the $\mathbb{SO}(3)$ plus operator, the wide hat $\langle \cdot \rangle$ refers to the skew-symmetric form of a vector, $\boldsymbol{\omega}_{\text{EN}}^{\text{N}}$ is the motion angular velocity¹² viewed in NED, $\mathbf{g}_{\text{c,MOD}}^{\text{N}}$ constitutes the gravity acceleration modeled by the navigation system, and $\mathbf{a}_{\text{cor}}^{\text{N}}$ represents the Coriolis acceleration also viewed in NED. In expression (11) \mathbf{u} is the known control or input vector and \mathbf{w} is the process noise¹³.

$$\dot{\mathbf{x}}(t) = [\Delta \dot{\mathbf{r}}_{\text{NB}}^{\text{B}} \ \dot{\boldsymbol{\omega}}_{\text{NB}}^{\text{B}} \ \dot{\mathbf{z}}]^{\text{T}} = \mathbf{f}(\mathbf{q}_{\text{NB}}(t) \oplus \Delta \mathbf{r}_{\text{NB}}^{\text{B}}(t), \boldsymbol{\omega}_{\text{NB}}^{\text{B}}(t), \mathbf{z}(t), \mathbf{u}(t), \mathbf{w}(t), t) \quad (11)$$

$$\dot{\mathbf{x}}_{1-3} = \Delta \dot{\mathbf{r}}_{\text{NB}}^{\text{B}} = \boldsymbol{\omega}_{\text{NB}}^{\text{B}} = \mathbf{x}_{4-6} \quad (12)$$

$$\dot{\mathbf{x}}_{7-9} = \dot{\mathbf{T}}^{\text{E,GDT}} = \left[\begin{array}{ccc} \mathbf{v}_2^{\text{N}} & \mathbf{v}_1^{\text{N}} & -\mathbf{v}_3^{\text{N}} \\ \left[\mathbf{N}(\varphi) + \mathbf{h} \right] \cos \varphi & \mathbf{M}(\varphi) + \mathbf{h} & \end{array} \right]^{\text{T}} \quad (13)$$

$$\dot{\mathbf{x}}_{10-12} = \dot{\mathbf{v}}^{\text{N}} = \mathbf{g}_{\mathbf{q}_{\text{NB}}} \oplus \Delta \mathbf{r}_{\text{NB}}^{\text{B}} * (\mathbf{f}_{\text{IB}}^{\text{B}}) - \hat{\boldsymbol{\omega}}_{\text{EN}}^{\text{N}} \mathbf{v}^{\text{N}} + \mathbf{g}_{\text{c,MOD}}^{\text{N}} - \mathbf{a}_{\text{cor}}^{\text{N}} \quad (14)$$

$$\dot{\mathbf{x}}_{\text{OTHER}} = \left[\dot{\boldsymbol{\omega}}_{\text{NB}}^{\text{B}} \ \dot{\mathbf{f}}_{\text{IB}}^{\text{B}} \ \dot{\mathbf{E}}_{\text{GYR}} \ \dot{\mathbf{E}}_{\text{ACC}} \ \dot{\mathbf{E}}_{\text{MAG}} \ \dot{\mathbf{B}}_{\text{DEV}}^{\text{N}} \right]^{\text{T}} = \mathbf{0}_{18} \quad (15)$$

$$\mathbf{u}(t) = \mathbf{0} \quad (16)$$

Its linearization results in the following system matrix $\mathbf{A}(t) = \partial \mathbf{f} / \partial \mathbf{x} (\mathbf{w} = \mathbf{0}) \in \mathbb{R}^{27 \times 27}$, in which appendix B describes the obtainment of the various Jacobians. Note that the linearization neglects the influence of the geodetic coordinates $\mathbf{T}^{\text{E,GDT}}$ on four different terms ($\dot{\mathbf{T}}^{\text{E,GDT}}$, $\boldsymbol{\omega}_{\text{EN}}^{\text{N}}$, $\mathbf{g}_{\text{c,MOD}}^{\text{N}}$, and $\mathbf{a}_{\text{cor}}^{\text{N}}$) present in the (11) differential equations, but includes the influence of the aircraft velocity \mathbf{v}^{N} on three of them (gravity does not depend on velocity). This is because the \mathbf{v}^{N} variation amount that can be experienced in a single state estimation step can have a significant influence on the values of the variables considered, while that of the geodetic coordinates $\mathbf{T}^{\text{E,GDT}}$ does not and hence can be neglected.

$$\dot{\mathbf{x}}(t) = \mathbf{A}(t) \mathbf{x}(t) + \mathbf{B}(t) \tilde{\mathbf{u}}(t) + \tilde{\mathbf{w}}(t) \quad (17)$$

$$\mathbf{A}_{1-3,4-6} = \frac{d \Delta \dot{\mathbf{r}}_{\text{NB}}^{\text{B}}}{d \boldsymbol{\omega}_{\text{NB}}^{\text{B}}} = \mathbf{I}_{3 \times 3} \quad (18)$$

$$\mathbf{A}_{7-9,10-12} = \frac{d \dot{\mathbf{T}}^{\text{E,GDT}}}{d \mathbf{v}^{\text{N}}} = \mathbf{J} \dot{\mathbf{T}}^{\text{E,GDT}}_{\mathbf{v}^{\text{N}}} \quad (19)$$

$$\mathbf{A}_{10-12,1-3} = \frac{d \dot{\mathbf{v}}^{\text{N}}}{d \Delta \mathbf{r}_{\text{NB}}^{\text{B}}} = \mathbf{J} \mathbf{g}_{\mathbf{q}_{\text{NB}} *}(\mathbf{f}_{\text{IB}}^{\text{B}}) \quad (20)$$

¹¹M and N represent the WGS84 radii of curvature of meridian and prime vertical, respectively.

¹²The motion angular velocity $\boldsymbol{\omega}_{\text{EN}}$ represents the rotation experienced by any object that moves without modifying its attitude with respect to the Earth surface.

¹³Note that although present, system noise $\mathbf{w}(t)$ is not shown in equations (12) through (15).

$$\mathbf{A}_{10-12,10-12} = \frac{d\hat{\mathbf{v}}^N}{d\mathbf{v}^N} = -\hat{\boldsymbol{\omega}}_{EN}^N + \hat{\mathbf{v}}^N \mathbf{J} \frac{\boldsymbol{\omega}_{EN}^N}{\mathbf{v}^N} - \mathbf{J} \frac{\mathbf{a}_{cor}^N}{\mathbf{v}^N} \quad (21)$$

$$\mathbf{A}_{10-12,13-15} = \frac{d\hat{\mathbf{v}}^N}{d\mathbf{f}_{IB}^B} = \mathbf{J} \frac{\mathbf{g}_{q_{NB}} \oplus \Delta \mathbf{r}_{NB}^B * (\mathbf{f}_{IB}^B)}{\mathbf{f}_{IB}^B} \quad (22)$$

$$A_{ij, OTHER} = 0 \quad (23)$$

$$\tilde{\mathbf{u}}(t) = \mathbf{0} \quad (24)$$

The discrete time nonlinear observations system (25) contains the observations provided by the different sensors, without any simplifications. New terminology includes the $\mathbb{SO}(3)$ group adjoint $\mathbf{Ad}()$, inverse adjoint $\mathbf{Ad}^{-1}()$, and inverse rotation $\mathbf{g}_*^{-1}()$ actions. In addition, $\boldsymbol{\omega}_{IE}^N$ represents the Earth angular velocity (viewed in NED) caused by its rotation around the \mathbf{i}_3^E axis at a constant rate ω_E , and \mathbf{v}_n represents the measurement or observation noise¹⁴.

$$\mathbf{y}_n = \mathbf{h}(\mathbf{q}_{NBn} \oplus \Delta \mathbf{r}_{NBn}^B, \boldsymbol{\omega}_{NBn}^B, \mathbf{z}_n, \mathbf{v}_n, t_n) \quad (25)$$

$$\tilde{\boldsymbol{\omega}}_{IB}^B = \boldsymbol{\omega}_{NB}^B + \mathbf{Ad}_{\mathbf{q}_{NB}}^{-1} \oplus \Delta \mathbf{r}_{NB}^B (\boldsymbol{\omega}_{IE}^N + \boldsymbol{\omega}_{EN}^N) + \mathbf{E}_{GYR} \quad (26)$$

$$\tilde{\mathbf{f}}_{IB}^B = \mathbf{f}_{IB}^B + \mathbf{E}_{ACC} \quad (27)$$

$$\tilde{\mathbf{B}}^B = \mathbf{g}_{\mathbf{q}_{NB}}^{-1} \oplus \Delta \mathbf{r}_{NB}^B * (\mathbf{B}_{MOD}^N - \mathbf{B}_{DEV}^N) + \mathbf{E}_{MAG} \quad (28)$$

$$\tilde{\mathbf{T}}^{E,GDT} = \mathbf{T}^{E,GDT} \quad (29)$$

$$\tilde{\mathbf{v}}^N = \mathbf{v}^N \quad (30)$$

Its linearization results in the following output matrix $\mathbf{H}_n = \partial \mathbf{h} / \partial \mathbf{x}_n (\mathbf{v}_n = \mathbf{0}) \in \mathbb{R}^{15 \times 27}$, in which appendix B describes the obtainment of the various Jacobians. As in the state system case above, the linearization also neglects the influence of the geodetic coordinates $\mathbf{T}^{E,GDT}$ on three different terms ($\boldsymbol{\omega}_{IE}^N$, $\boldsymbol{\omega}_{EN}^N$, and \mathbf{B}_{MOD}^N) present in the (25) observation equations. Note that it is not necessary to evaluate the observations input vector \mathbf{z}_n as it plays no role in the solution [2, 10].

$$\mathbf{y}_n \approx \mathbf{H}_n \mathbf{x}_n + \mathbf{z}_n + \tilde{\mathbf{v}}_n \quad (31)$$

$$\mathbf{H}_{1-3,1-3} = \frac{d\tilde{\boldsymbol{\omega}}_{IB}^B}{d\Delta \mathbf{r}_{NB}^B} = \mathbf{J} \frac{\mathbf{Ad}_{\mathbf{q}_{NB}}^{-1} (\boldsymbol{\omega}_{IE}^N + \boldsymbol{\omega}_{EN}^N)}{\mathcal{R}_{NB}} \quad (32)$$

$$\mathbf{H}_{1-3,4-6} = \frac{d\tilde{\boldsymbol{\omega}}_{IB}^B}{d\boldsymbol{\omega}_{NB}^B} = \mathbf{I}_{3 \times 3} \quad (33)$$

$$\mathbf{H}_{1-3,10-12} = \frac{d\tilde{\boldsymbol{\omega}}_{IB}^B}{d\mathbf{v}^N} = \mathbf{J} \frac{\mathbf{Ad}_{\mathbf{q}_{NB}}^{-1} \oplus \Delta \mathbf{r}_{NB}^B (\boldsymbol{\omega}_{EN}^N)}{\boldsymbol{\omega}_{EN}^N} \mathbf{J} \frac{\boldsymbol{\omega}_{EN}^N}{\mathbf{v}^N} \quad (34)$$

$$\mathbf{H}_{1-3,16-18} = \frac{d\tilde{\boldsymbol{\omega}}_{IB}^B}{d\mathbf{E}_{GYR}} = \mathbf{I}_{3 \times 3} \quad (35)$$

$$\mathbf{H}_{4-6,13-15} = \frac{d\tilde{\mathbf{f}}_{IB}^B}{d\mathbf{f}_{IB}^B} = \mathbf{I}_{3 \times 3} \quad (36)$$

$$\mathbf{H}_{4-6,19-21} = \frac{d\tilde{\mathbf{f}}_{IB}^B}{d\mathbf{E}_{ACC}} = \mathbf{I}_{3 \times 3} \quad (37)$$

$$\mathbf{H}_{7-9,1-3} = \frac{d\tilde{\mathbf{B}}^B}{d\Delta \mathbf{r}_{NB}^B} = \mathbf{J} \frac{\mathbf{g}_{\mathbf{q}_{NB}}^{-1} * (\mathbf{B}_{MOD}^N - \mathbf{B}_{DEV}^N)}{\mathcal{R}_{NB}} \quad (38)$$

$$\mathbf{H}_{7-9,22-24} = \frac{d\tilde{\mathbf{B}}^B}{d\mathbf{E}_{MAG}} = \mathbf{I}_{3 \times 3} \quad (39)$$

$$\mathbf{H}_{7-9,25-27} = \frac{d\tilde{\mathbf{B}}^B}{d\mathbf{B}_{DEV}^N} = -\mathbf{J} \frac{\mathbf{g}_{\mathbf{q}_{NB}}^{-1} \oplus \Delta \mathbf{r}_{NB}^B * (\mathbf{B}_{DEV}^N)}{\mathbf{B}_{DEV}^N} \quad (40)$$

$$\mathbf{H}_{10-12,7-9} = \frac{d\tilde{\mathbf{T}}^{E,GDT}}{d\mathbf{T}^{E,GDT}} = \mathbf{I}_{3 \times 3} \quad (41)$$

$$\mathbf{H}_{13-15,10-12} = \frac{d\tilde{\mathbf{v}}^N}{d\mathbf{v}^N} = \mathbf{I}_{3 \times 3} \quad (42)$$

¹⁴Note that although present, measurement noise \mathbf{v}_n is not shown in equations (26) through (30).

$$H_{ij, \text{OTHER}} = 0 \quad (43)$$

Based on the above linearized continuous state system and discrete observations, each step within the the classical EKF implementation [2, 10] results in estimations for both the state vector $\hat{\mathbf{x}}_n = [\Delta\hat{\mathbf{r}}_{\text{NBN}}^B \ \hat{\boldsymbol{\omega}}_{\text{NBN}}^B \ \hat{\mathbf{z}}_n]^T$ as well as its covariance \mathbf{P}_n . Note that the definition of the covariance matrix is a combination of that of its Euclidean components and its local Lie counterparts [2], with additional combined members¹⁵:

$$\mathbf{P}_n = \begin{bmatrix} \mathbf{C}_{\mathcal{R}\mathcal{R},n}^{\mathcal{R}} & \mathbf{C}_{\mathcal{R}\mathbf{p},n}^{\mathcal{R}} \\ \mathbf{C}_{\mathbf{p}\mathcal{R},n}^{\mathcal{R}} & \mathbf{C}_{\mathbf{p}\mathbf{p},n} \end{bmatrix} \in \mathbb{R}^{27 \times 27} \quad (44)$$

$$\mathbf{C}_{\mathcal{R}\mathcal{R},n}^{\mathcal{R}} = E[\Delta\mathbf{r}_{\text{NBN}}^B \Delta\mathbf{r}_{\text{NBN}}^{B,T}] = E[(\mathcal{R}_{\text{NBN}} \ominus \boldsymbol{\mu}_{\mathcal{R},\text{NBN}}) (\mathcal{R}_{\text{NBN}} \ominus \boldsymbol{\mu}_{\mathcal{R},\text{NBN}})^T] \in \mathbb{R}^{3 \times 3} \quad (45)$$

$$\mathbf{C}_{\mathcal{R}\mathbf{p},n}^{\mathcal{R}} = E[\Delta\mathbf{r}_{\text{NBN}}^B (\mathbf{p}_n - \boldsymbol{\mu}_{\mathbf{p},n})^T] = E[(\mathcal{R}_{\text{NBN}} \ominus \boldsymbol{\mu}_{\mathcal{R},\text{NBN}}) (\mathbf{p}_n - \boldsymbol{\mu}_{\mathbf{p},n})^T] \in \mathbb{R}^{3 \times 24} \quad (46)$$

$$\mathbf{C}_{\mathbf{p}\mathcal{R},n}^{\mathcal{R}} = E[(\mathbf{p}_n - \boldsymbol{\mu}_{\mathbf{p},n}) \Delta\mathbf{r}_{\text{NBN}}^{B,T}] = E[(\mathbf{p}_n - \boldsymbol{\mu}_{\mathbf{p},n}) (\mathcal{R}_{\text{NBN}} \ominus \boldsymbol{\mu}_{\mathcal{R},\text{NBN}})^T] \in \mathbb{R}^{24 \times 3} \quad (47)$$

$$\mathbf{C}_{\mathbf{p}\mathbf{p},n} = E[(\mathbf{p}_n - \boldsymbol{\mu}_{\mathbf{p},n}) (\mathbf{p}_n - \boldsymbol{\mu}_{\mathbf{p},n})^T] \in \mathbb{R}^{24 \times 24} \quad (48)$$

In the modified EKF scheme suggested here, each estimation step concludes by resetting the estimation of the tangent space perturbation $\Delta\hat{\mathbf{r}}_{\text{NBN}}^B$ to zero while modifying the estimations for the Lie rotation group element $\hat{\mathcal{R}}_{\text{NBN}}$ and the error covariance \mathbf{P}_n accordingly¹⁶. Note that the accuracy of the linearizations required to obtain the **A** and **H** system and output matrices are based on first order Taylor expansions, which are directly related to the size of the tangent space perturbations. Although it is not strictly necessary to reset the perturbations in every EKF cycle, the accuracy of the whole state estimation process is improved by maintaining the perturbations as small as possible, so it is recommended to never bypass the reset step.

Taking into account that the rotation element is going to be updated per (51), the error covariance is propagated to the new rotation element as follows [2], where the Jacobian is provided by (59) within appendix B:

$$\mathbf{P}_n \leftarrow \mathbf{D} \mathbf{P}_n \mathbf{D}^T \quad (49)$$

$$\mathbf{D} = \begin{bmatrix} \mathbf{J} \hat{\mathcal{R}}_{\text{NBN}} \oplus \Delta\hat{\mathbf{r}}_{\text{NBN}}^B & \mathbf{0}_{3 \times 24} \\ \hat{\mathcal{R}}_{\text{NBN}} & \mathbf{I}_{24 \times 24} \\ \mathbf{0}_{24 \times 3} & \end{bmatrix} \in \mathbb{R}^{27 \times 27} \quad (50)$$

Last, the rotation element is propagated by means of the local rotation vector perturbation, which is itself reset to zero:

$$\hat{\mathbf{q}}_{\text{NBN}} \leftarrow \hat{\mathbf{q}}_{\text{NBN}} \oplus \Delta\hat{\mathbf{r}}_{\text{NBN}}^B \quad (51)$$

$$\Delta\hat{\mathbf{r}}_{\text{NBN}}^B \leftarrow \mathbf{0}_3 \quad (52)$$

Different position (geodetic coordinates) and ground velocity system noise values are employed depending on whether the measurements are provided by the GNSS receiver or the VVS. Lower geodetic coordinates system noise values are employed when GNSS signals are available, as the objective is for the solution to avoid position jumps by smoothly following the state equations and only slightly updating the position based on the GNSS observations to avoid any position drift on the long term. When the position observations are instead supplied by the VVS, higher system noise values are employed so the EKF relies more on the observations and less on the integration. Note that the VVS velocity observations are very noisy because of (2), so it is better if the EKF closely adheres to the position observations that originate at the IA-VNS, correcting in each step as necessary.

6 Fully Integrated Visual Inertial Navigation System

The fully integrated VINS combines the visual (IA-VNS) and inertial (VA-INS) systems in such a way that each assists the other while being simultaneously controlled by it, as depicted in figure 4. As the VINS needs to estimate

¹⁵ \ominus represents the $\text{SO}(3)$ rotation group minus operator [2, 4].

¹⁶ The estimations for angular velocity $\hat{\boldsymbol{\omega}}_{\text{NBN}}^B$ and the Euclidean components $\hat{\mathbf{z}}_n$ are not modified.

the state $\hat{\mathbf{x}} = \mathbf{x}_{\text{EST}}$ at every $t_n = t_s = n \cdot \Delta t_{\text{EST}} = s \cdot \Delta t_{\text{SENSED}}$, it has three different operation modes, depending not only on whether GNSS signals are available or not, but also on whether there exists a position and ground velocity observation at the execution time $t_n = t_s$:

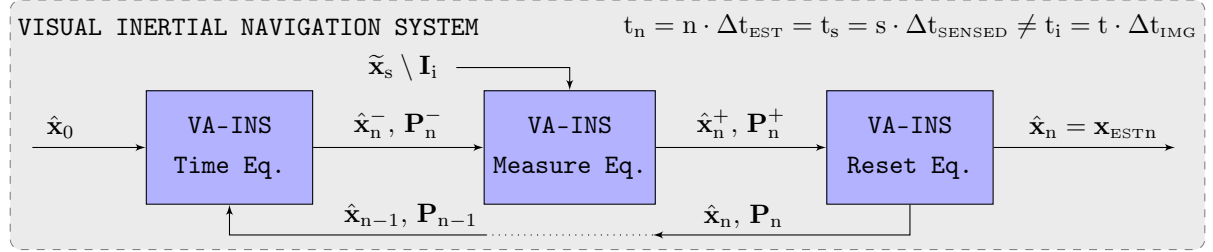


Figure 5: VINS flow diagram when $t_n = t_s \neq t_i$

- Given the operating frequencies of the different sensors (table 1), most VINS executions (ninety-nine out of one hundred for GNSS-Based navigation, nine out of ten in case of GNSS-Denied conditions) can not rely on the position and ground velocity observations provided by either the GNSS receiver or the VVS. As graphically depicted in figure 5, these VINS executions rely on the proposed navigation filter (section 5), which follows the modified Lie algebra EKF scheme consisting on the successive application (after initialization) of its time update, measurement update, and reset equations¹⁷. Note that the filter observation system (25) needs to be modified to remove (29) and (30) as there are no GNSS receiver or VVS observations available.

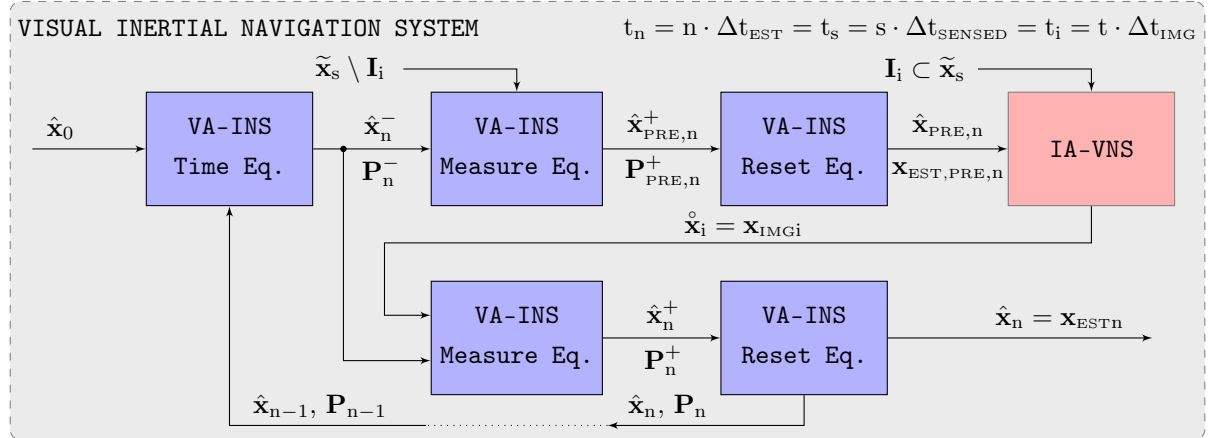


Figure 6: VINS flow diagram when $t_n = t_s = t_i$

- GNSS-Denied executions for which the VVS position and ground velocity observations are available at the required time ($t_n = n \cdot \Delta t_{\text{EST}} = t_i = i \cdot \Delta t_{\text{IMG}}$) instead rely on the more complex scheme depicted in figure 6. Note that this case only occurs in one out of ten executions for GNSS-Denied conditions. The first part of the process is exactly the same as in the previous case, and results in a preliminary estimated state that does not employ the VVS measurements (this is, does not employ the \mathbf{I}_i image corresponding to t_i nor the IA-VNS algorithms), denoted $\hat{\mathbf{x}}_{\text{PRE}}(t_n) = \mathbf{x}_{\text{EST,PRE}}(t_n)$ in the figure to avoid confusion.

This preliminary estimation, together with the \mathbf{I}_i image, is then passed to the IA-VNS as described in [6] to obtain a visual state $\dot{\mathbf{x}}(t_i) = \mathbf{x}_{\text{IMG}}(t_i)$, which as explained in section 4 is equivalent to the VVS position and ground velocity outputs. Only then it is possible to apply the complete VA-INS navigation filter measurement update and reset equations for a second time to obtain the final state estimation $\hat{\mathbf{x}}(t_n) = \mathbf{x}_{\text{EST}}(t_n)$.

- GNSS-Based executions for which the GNSS receiver position and ground velocity observations are available at the required time ($t_n = n \cdot \Delta t_{\text{EST}} = t_g = g \cdot \Delta t_{\text{GNSS}}$). This case, which only occurs in one out of a hundred executions when GNSS signals are available and is shown in figure 7, is in fact very similar to the first one

¹⁷As discussed in section 5, the reset step is not present in a fully Euclidean EKF scheme.

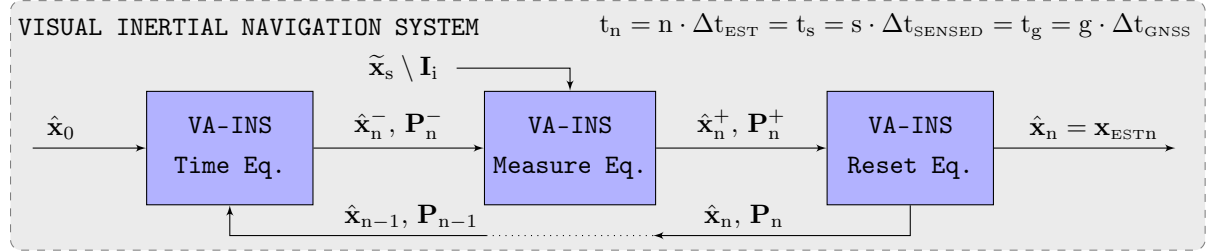


Figure 7: VINS flow diagram when $t_n = t_s = t_g$

above, with the only difference that the navigation filter observation system (25) can be applied as written since it includes the GNSS receiver observations.

7 Testing: High Fidelity Simulation and Scenarios

To evaluate the performance of the proposed navigation algorithms, this article relies on Monte Carlo simulations consisting of one hundred runs each of two different scenarios based on the high fidelity stochastic flight simulator graphically depicted in figure 8. Described in detail in [12] and with its open source C++ implementation available in [1], the simulator models the flight in varying weather and turbulent conditions of a fixed wing piston engine autonomous UAV.

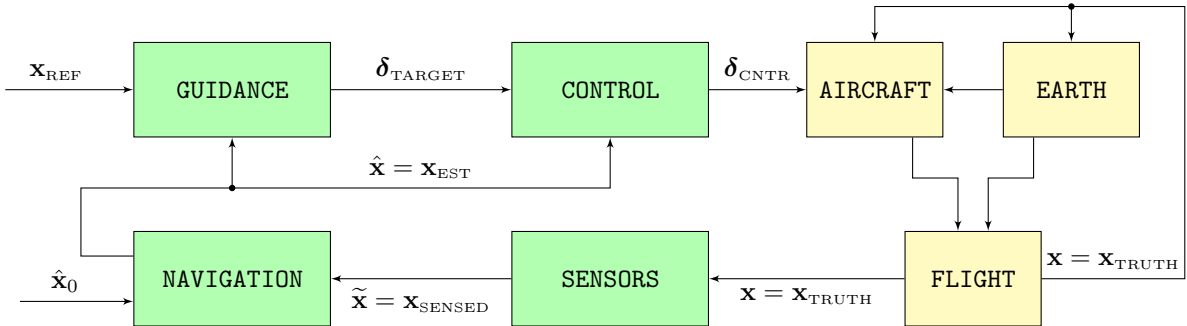


Figure 8: Components of the high fidelity simulation

The simulator consists of two distinct processes. The first, represented by the yellow blocks on the right of figure 8, models the physics of flight and the interaction between the aircraft and its surroundings that results in the real aircraft trajectory $\mathbf{x} = \mathbf{x}_{\text{TRUTH}}$; the second, represented by the green blocks on the left, contains the aircraft systems in charge of ensuring that the resulting trajectory adheres as much as possible to the mission objectives. It includes the different sensors whose output comprise the sensed trajectory $\tilde{\mathbf{x}} = \mathbf{x}_{\text{SENSED}}$, the navigation system in charge of filtering it to obtain the estimated trajectory $\hat{\mathbf{x}} = \mathbf{x}_{\text{EST}}$, the guidance system that converts the reference objectives \mathbf{x}_{REF} into the control targets δ_{TARGET} , and the control system that adjusts the position of the throttle and aerodynamic control surfaces δ_{CNTR} so the estimated trajectory $\hat{\mathbf{x}}$ is as close as possible to the reference objectives \mathbf{x}_{REF} . Table 1 lists the working frequencies of the various blocks represented in figure 8.

All components of the flight simulator have been modeled with as few simplifications as possible to increase the realism of the results, as explained in [9, 12]. With the exception of the aircraft performances and its control system, which are deterministic, all other simulator components are treated as stochastic and hence vary from one execution to the next, enhancing the significance of the Monte Carlo simulation results.

Most VIO packages discussed in appendix A include in their release articles an evaluation when applied to the EuRoC Micro Air Vehicle (MAV) data sets¹⁸ [13], and so do independent articles such as [14]. The algorithms presented in this article are hence tested through simulation under two different scenarios designed to analyze the

¹⁸These data sets contain perfectly synchronized stereo images, IMU measurements, and ground truth readings obtained with laser, for eleven different indoor trajectories flown with a MAV, each with a duration in the order of two minutes and a total distance in

consequences of losing the **GNSS** signals for long periods of time. Although a short summary is included below, detailed descriptions of the mission, weather, and wind field employed in each scenario can be found in [12]. Most parameters comprising the scenario are defined stochastically, resulting in different values for every execution. Note that all results shown in section 8 are based on Monte Carlo simulations comprising one hundred runs of each scenario, testing the sensitivity of the proposed navigation algorithms to a wide variety of values in the parameters.

- Scenario #1 has been defined with the objective of adequately representing the challenges faced by an autonomous fixed wing UAV that suddenly cannot rely on **GNSS** and hence changes course to reach a pre-defined recovery location situated at approximately one hour of flight time. In the process, in addition to executing an altitude and airspeed adjustment, the autonomous aircraft faces significant weather and wind field changes that make its **GNSS**-Denied navigation even more challenging.

With respect to the mission, the stochastic parameters include the initial airspeed, pressure altitude, and bearing ($v_{TAS,INI}$, $H_{P,INI}$, χ_{INI}), their final values ($v_{TAS,END}$, $H_{P,END}$, χ_{END}), and the time at which each of the three maneuvers is initiated¹⁹. The scenario lasts for $t_{END} = 3800$ s, while the **GNSS** signals are lost at $t_{GNSS} = 100$ s.

The wind field is also defined stochastically, as its two parameters (speed and bearing) are constant both at the beginning ($v_{WIND,INI}$, $\chi_{WIND,INI}$) and conclusion ($v_{WIND,END}$, $\chi_{WIND,END}$) of the scenario, with a linear transition in between. The specific times at which the wind change starts and concludes also vary stochastically among the different simulation runs. As described in [12], the turbulence remains strong throughout the whole scenario, but its specific values also vary stochastically from one execution to the next.

A similar linear transition occurs with the temperature and pressure offsets that define the atmospheric properties [15], as they are constant both at the start (ΔT_{INI} , Δp_{INI}) and end (ΔT_{END} , Δp_{END}) of the flight. In contrast with the wind field, the specific times at which the two transitions start and conclude are not only stochastic but also different from each other.

- Scenario #2 represents the challenges involved in continuing with the original mission upon the loss of the **GNSS** signals, executing a series of continuous turn maneuvers over a relatively short period of time with no atmospheric or wind variations. As in scenario #1, the **GNSS** signals are lost at $t_{GNSS} = 100$ s, but the scenario duration is shorter ($t_{END} = 500$ s). The initial airspeed and pressure altitude ($v_{TAS,INI}$, $H_{P,INI}$) are defined stochastically and do not change throughout the whole scenario; the bearing however changes a total of eight times between its initial and final values, with all intermediate bearing values as well as the time for each turn varying stochastically from one execution to the next. Although the same turbulence is employed as in scenario #1, the wind and atmospheric parameters ($v_{WIND,INI}$, $\chi_{WIND,INI}$, ΔT_{INI} , Δp_{INI}) remain constant throughout scenario #2.

8 Navigation System Error in **GNSS**-Denied Conditions

This section presents the results obtained with the proposed fully integrated visual inertial navigation system (**VINS**) when executing Monte Carlo simulations of the two **GNSS**-Denied scenarios introduced in section 7, each consisting of one hundred executions. They are compared with those of the standalone inertial and visual systems (**INS** and **VNS**), as well as those of the inertially assisted **VNS** or **IA-VNS** described in section 3. The tables below contain the *navigation system error*²⁰ (**NSE**) incurred by the various navigation systems (and accordingly denoted

the order of 100 m. This fact by itself indicates that the target application of exiting **VI0** implementations differs significantly from the main focus of this article, as there may exist accumulating errors that are completely non discernible after such short periods of time, but that grow non linearly and have the capability of inducing significant pose errors when the aircraft remains aloft for long periods of time.

¹⁹Turns are executed with a bank angle of $\xi_{TURN} = \pm 10^\circ$, altitude changes employ an aerodynamic path angle of $\gamma_{TAS,CLIMB} = \pm 2^\circ$, and airspeed modifications are automatically executed by the control system as set-point changes.

²⁰The **NSE** is the difference between the real states (\mathbf{x}) and their estimation ($\hat{\mathbf{x}}$ or $\ddot{\mathbf{x}}$) by the navigation system.

as **INSE**, **VNSE**, **IA-VNSE**, and **VINSE**) at the conclusion of the two **GNSS**-Denied scenarios, represented by the mean, standard deviation, and maximum value of the estimation errors. In addition, the figures depict the variation with time of the **NSE** mean (solid line) and standard deviation (dashed lines) for the one hundred executions. The following remarks are necessary:

- The results obtained with the **INS** under the same two **GNSS**-Denied scenarios are discussed in [5]. The attitude **INSE** does not drift and is bounded by the quality of the onboard sensors, ensuring the aircraft can remain aloft for as long as there is fuel available. The vertical position and ground velocity **INSEs** are also bounded by atmospheric physics and do not drift; their estimation errors depend on the atmospheric pressure offset and wind field changes that occur since the **GNSS** signals are lost. On the other hand, the horizontal position **INSE** drifts as a consequence of integrating the ground velocity without absolute observations. Of the six $\mathbb{SE}(3)$ degrees of freedom (three for attitude, two for horizontal position, one for altitude), the **INS** is hence capable of successfully estimating four of them in **GNSS**-Denied conditions.
- Visual navigation systems (**VNS**, **IA-VNS**, and the fully integrated **VINS**) are only necessary to reduce the estimation error in the two remaining degrees of freedom (the horizontal position). Although they all estimate the complete six dimensional aircraft pose, their attitude and altitude estimations shall only be understood as a means to provide more accurate horizontal position estimations, which represents their sole objective.
- The results obtained with the **VNS** and **IA-VNS** under the same two scenarios are discussed in [6]. Even though the **VNSE** slowly drifts in all six degrees of freedom, the addition of **INS** based priors enables the **IA-VNS** to reduce the drift in all six dimensions, with the resulting horizontal position **IA-VNSE** being just a fraction of the **INSE**. The attitude and altitude **IA-VNSEs**, although improved when compared to the **VNSEs**, are qualitatively inferior to the driftless **INSEs**.
- The main focus of this article lies in the horizontal position estimation improvements that occur when the navigation filter **EKF** can make use of the **VVS** observations provided by the **IA-VNS** to replace those of the **GNSS** receiver.

8.1 Body Attitude Estimation

Table 3 shows the **NSE** at the conclusion of both scenarios for the norm of the rotation vector between the real body attitude \mathbf{q}_{NB} and its estimations, $\hat{\mathbf{q}}_{NB}$ or $\mathring{\mathbf{q}}_{NB}$. The errors hence can be formally written as $\|\Delta\hat{\mathbf{r}}_{NB}^B\| = \|\hat{\mathbf{q}}_{NB} \ominus \mathbf{q}_{NB}\|$ or $\|\Delta\mathring{\mathbf{r}}_{NB}^B\| = \|\mathring{\mathbf{q}}_{NB} \ominus \mathbf{q}_{NB}\|$, where \ominus represents the $\mathbb{SO}(3)$ minus operator [2, 4]. In addition, figures 9 and 10 depict the variation with time of the body attitude **NSE** for both scenarios.

Scenario (t_{END})		NSE	VNSE	IA-VNSE	VINSE
	[°]	$\ \Delta\hat{\mathbf{r}}_{NB}^B\ $	$\ \Delta\mathring{\mathbf{r}}_{NB}^B\ $	$\ \Delta\mathring{\mathbf{r}}_{NB}^B\ $	$\ \Delta\hat{\mathbf{r}}_{NB}^B\ $
#1	mean	0.158	0.296	0.218	0.100
	std	0.114	0.158	0.103	0.059
	max	0.611	0.791	0.606	0.328
#2	mean	0.128	0.253	0.221	0.107
	std	0.078	0.161	0.137	0.068
	max	0.369	0.730	0.788	0.377

Table 3: Aggregated final body attitude **INSE**, **VNSE**, **IA-VNSE**, and **VINSE** (100 runs)

- After a short transition period following the introduction of **GNSS**-Denied conditions at $t_{GNSS} = 100$ s, the body attitude **INSE** (blue lines) does not experience any drift with time in either scenario, and is bounded by the quality of the onboard sensors and the inertial navigation algorithms [5]. The bounded attitude implies that the UAV can remain aloft without **GNSS** signals for as long as it has fuel.
- The body attitude **VNSE** (red lines) experiences a slight drift with time in both scenarios, with most of

the error attributed to the roll-in and roll-out maneuvers within the initial turn [6]. The lack of error growth during most of scenario #2 is caused by the trajectories being so twisted (refer to [12]) that terrain zones previously mapped reappear in the camera field of view during the consecutive turns, and are hence employed by **SVO** as absolute references, resulting in a much better attitude estimation that what would occur under more spaced turns.

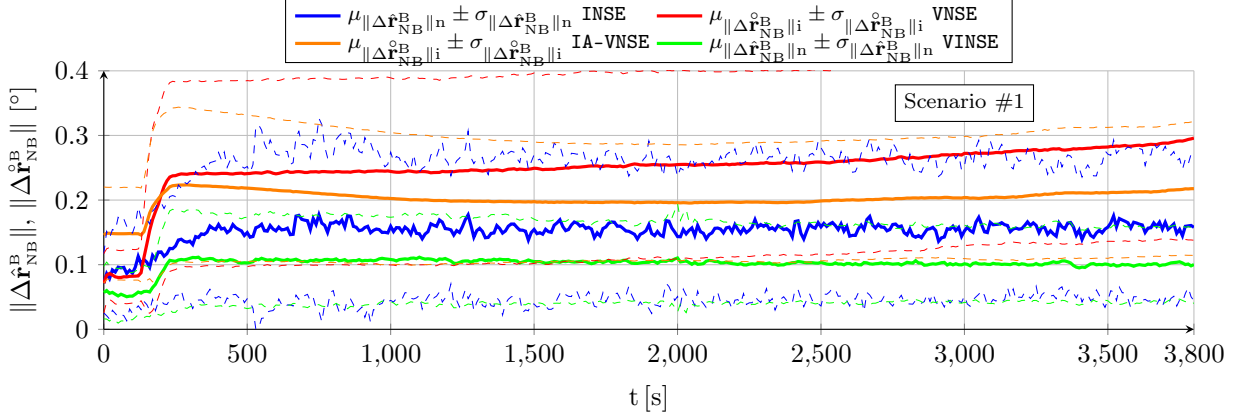


Figure 9: Body attitude INSE, VNSE, IA-VNSE, and VINSE for scenario #1 (100 runs)

- The **IA-VNSE** (orange lines) shows significant improvements over the **VNSE** as the **IA-VNS** successfully limits the deviation between the visual pitch and bank estimations with respect to the inertial ones provided by the **INS** (figure 3) [6]. The improvement is more significant in the case of scenario #1 because the **IA-VNS** algorithms are by design slow adjustments that require significant time to slowly correct the deviations [6]. Note that the higher **IA-VNSEs** at the beginning of both scenarios are also caused by the **IA-VNS** initialization adjustments [6].

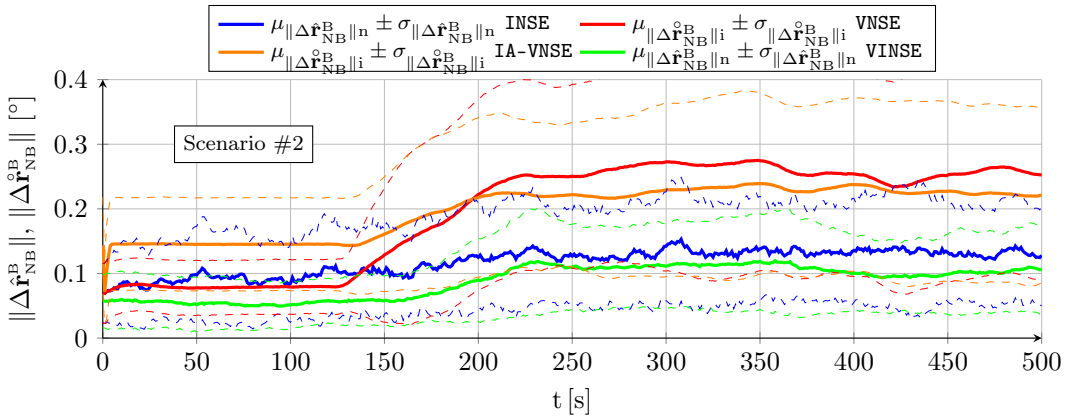


Figure 10: Body attitude INSE, VNSE, IA-VNSE, and VINSE for scenario #2 (100 runs)

- The fully integrated **VINSE** shows sustained and significant body attitude estimation improvements with respect to the **INSE** in both scenarios, which can be attributed to various factors. On one hand, the proposed navigation filter successfully merges the incremental horizontal displacement observations supplied by the **VVS** with the bearing provided by the magnetometers, resulting in better yaw estimations. In addition, the absence of simplifications in the **EKF** observation equations²¹ ensures that the benefits also reach the already accurate inertial pitch and bank angle estimations. Additional body attitude estimation improvements are achieved by closing the loop (figure 4) and directly employing the increasingly accurate body attitude inertial **VA-INS** estimations to feed the **IA-VNS** (section 6).

²¹Note that in the absence of both **GNSS** receiver and **VVS** observations, the filter observation equations need to be simplified to protect the filter behavior from the negative effects of inaccurate velocity and position estimations, as discussed in [5].

8.2 Vertical Position Estimation

Table 4 contains the vertical position NSE ($\Delta\hat{h} = \hat{h} - h$, $\Delta\hat{h} = \hat{h} - h$) at the conclusion of both scenarios, which can be considered unbiased or zero mean in all eight cases (two scenarios and four estimation methods) as the mean is always significantly lower than both the standard deviation or the maximum error value. The geometric altitude NSE evolution with time is depicted in figures 11 and 12, respectively.

Scenario (t_{END})	INSE	VNSE	IA-VNSE	VINSE	
	[m]	$\Delta\hat{h}$	$\Delta\hat{h}$	$\Delta\hat{h}$	
#1	mean	-4.18	+82.91	+22.86	-3.97
	std	25.78	287.58	49.17	26.12
	max	-70.49	+838.32	+175.76	-70.47
#2	mean	+0.76	+3.45	+3.59	+0.74
	std	7.55	20.56	13.01	7.60
	max	-19.86	+72.69	+71.64	-18.86

Table 4: Aggregated final vertical position INSE, VNSE, IA-VNSE, and VINSE (100 runs)

- The geometric altitude INSE (blue lines) is bounded by the change in atmospheric pressure offset [15] since the time the GNSS signals are lost [5].
- The vertical position VNSE (red lines) is significantly worse than the INSE both qualitatively and quantitatively [6], experiencing a continuous drift or error growth with time; the errors are logically bigger for scenario #1 because of its much longer duration. Most of this drift results from adding the estimated relative pose between two consecutive images to a pose (that of the previous image) with an attitude that already possesses a small pitch error (refer to the attitude estimation analysis in section 8.1). Note that even a fraction of a degree deviation in pitch can result in hundreds of meters in vertical error when applied to the total distance flown in scenario #1. As shown in figure 12, the vertical position VNSE grows more slowly in the second half of scenario #2 because, as explained in section 8.1 above, continuous turn maneuvers cause previously mapped terrain points to reappear in the camera field of view, stopping the growth in the attitude error (pitch included), which indirectly has the effect of slowing the growth in altitude estimation error.

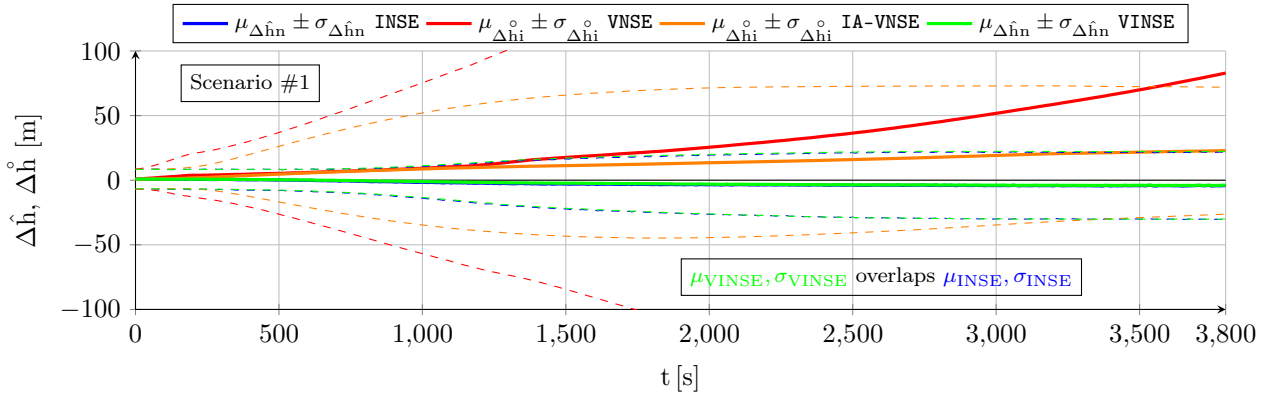


Figure 11: Vertical position INSE, VNSE, IA-VNSE, and VINSE for scenario #1 (100 runs)

- The IA-VNSE (orange lines) experiences a drastic reduction with respect to the VNSE in the case of scenario #1, where its extended duration allows the IA-VNS slow pose adjustments to accumulate into significant altitude corrections over time, and less pronounced but nevertheless significant for scenario #2 [6]. Although it can not be compared with the vertical position results obtained with the INS, note that its main purpose is to improve the fit between the real terrain and the map generated by SVO, resulting in horizontal position improvements (section 8.3).
- The fully integrated VINS (green lines) vertical position estimation accuracy is virtually the same as that

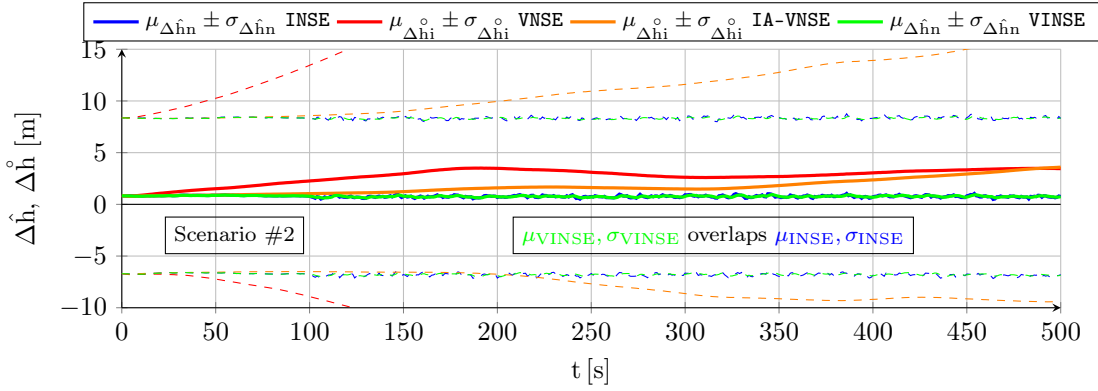


Figure 12: Vertical position INSE, VNSE, IA-VNSE, and VINSE for scenario #2 (100 runs)

of the INS because the proposed navigation filter described in section 5 relies on freezing the pressure offset estimation $\Delta\hat{p}$ when the GNSS signals are lost, exactly the same as the INS filter [5]. The resulting altitude estimations are unbiased and bounded, with an error that depends on the change in pressure offset since the time the GNSS are lost.

8.3 Horizontal Position Estimation

Table 5 lists the mean, standard deviation, and maximum value of the horizontal position NSEs at the conclusion of the two scenarios, both in length units and as a percentage of the total distance flown in GNSS-Denied conditions. The horizontal position estimation capabilities of the four considered navigation systems share the fact that all of them exhibit an unrestrained drift or growth with time, as shown in figures 13 and 14.

Scenario (t_{END})		INSE		VNSE		IA-VNSE		VINSE		
		Distance	$\Delta\hat{x}_{\text{HOR}}$		$\Delta\hat{x}_{\text{HOR}}$	$\Delta\hat{x}_{\text{HOR}}$		$\Delta\hat{x}_{\text{HOR}}$		
			[m]	[m]		[m]	[%]	[m]	[%]	
#1	mean	107873	7276	7.10	4179	3.82	488	0.46	207	0.19
	std	19756	4880	5.69	3308	2.73	350	0.31	185	0.15
	max	172842	25288	32.38	21924	14.22	1957	1.48	1257	1.09
#2	mean	14198	216	1.52	251	1.77	33	0.23	18	0.13
	std	1176	119	0.86	210	1.48	26	0.18	9	0.07
	max	18253	586	4.38	954	7.08	130	0.98	43	0.33

Table 5: Aggregated final horizontal position INSE, VNSE, IA-VNSE, and VINSE (100 runs)

- In the case of the standalone INS (blue lines), the drift is caused by integrating the bounded horizontal velocity estimations without any absolute observations (which in normal circumstances are provided by the GNSS receiver) [5], resulting in the aircraft incurring in position errors that preclude inertial systems as a valid navigation source for GNSS-Denied navigation. Note that as explained in [5], the errors (percentage wise) are much lower in scenario #2 because it does not include any wind variations, resulting in a more accurate ground velocity (and hence horizontal position) estimation than what could be achieved otherwise.
- The horizontal position VNSE (red lines) also shows a continuous error accumulation caused by the concatenation of the relative poses between consecutive images without absolute references, coupled with additional inaccuracies traced to the estimation of the aircraft height over the terrain during the visual odometry initialization [6]. Figure 14 shows the same slope diminution in the second half of the scenario discussed in previous sections caused by previously mapped terrain points reappearing in the camera field of view as a consequence of the continuous turns present in scenario #2.
- The IA-VNS (orange lines) results in major horizontal position estimation improvements over the VNS in both scenarios, as the mean of the final errors diminishes from 3.82 to 0.46 % for scenario #1, and from

1.77 to 0.23 % for scenario #2. The repeatability of the results also improves, as the standard deviation falls from 2.73 to 0.31 % and from 1.48 to 0.18 % for both scenarios. As explained in [6], the reason for this improvement lies in that the improved IA-VNS attitude and altitude estimations discussed in sections 8.1 and 8.2 enable **SVO** to build a better map of the terrain, resulting in an improved fit between the ground terrain and associated 3D points depicted in the images on one side, and the estimated aircraft pose indicating the position and attitude from where the images are taken on the other.

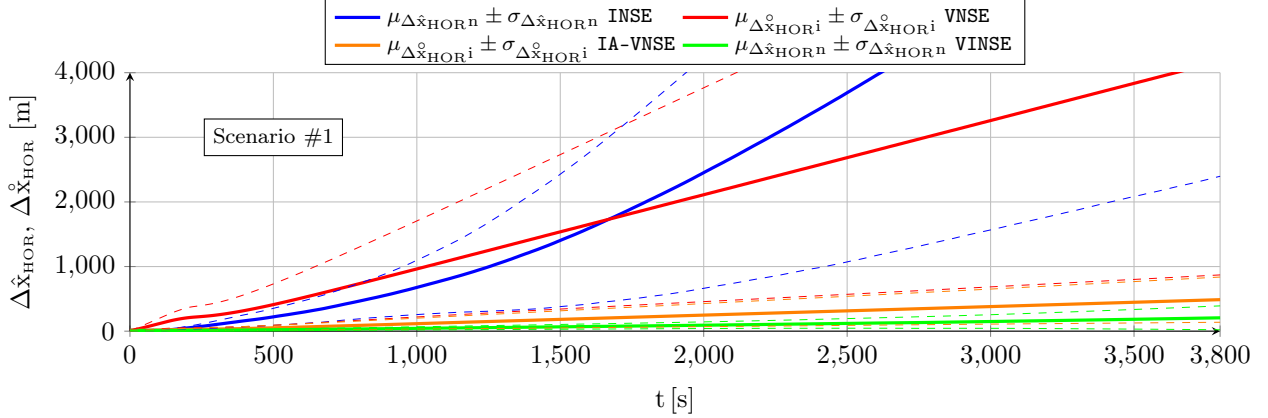


Figure 13: Horizontal position INSE, VNSE, IA-VNSE, and VINSE for scenario #1 (100 runs)

- In the case of the fully integrated VINS (green lines), the objective when supplying the proposed navigation filter with the VVS observations (equivalent to the IA-VNS incremental displacement estimations) is to employ more accurate observation equations within the EKF as there is no longer a need to protect the filter from the negative effects of inaccurate velocity and position values, as in the case of the INS filter [5]. This improved design enables significant improvements in body attitude (section 8.1) because the filter is capable of incorporating the whole IA-VNS horizontal position improvements into the EKF filter. In a positive feedback loop, the VINS then capitalizes on its more accurate attitude estimations to further improve its internal IA-VNS horizontal position estimations (figure 4). Although small in absolute terms (length units) when compared to the much higher errors encountered in previous phases, percentage-wise the horizontal position improvements obtained when closing the loop are very significant, as the final error mean diminishes from 0.46 to 0.19 % for scenario #1, and from 0.23 to 0.13 % for #2, while the standard deviation also falls from 0.31 to 0.15 %, and from 0.18 to 0.07 %, respectively.

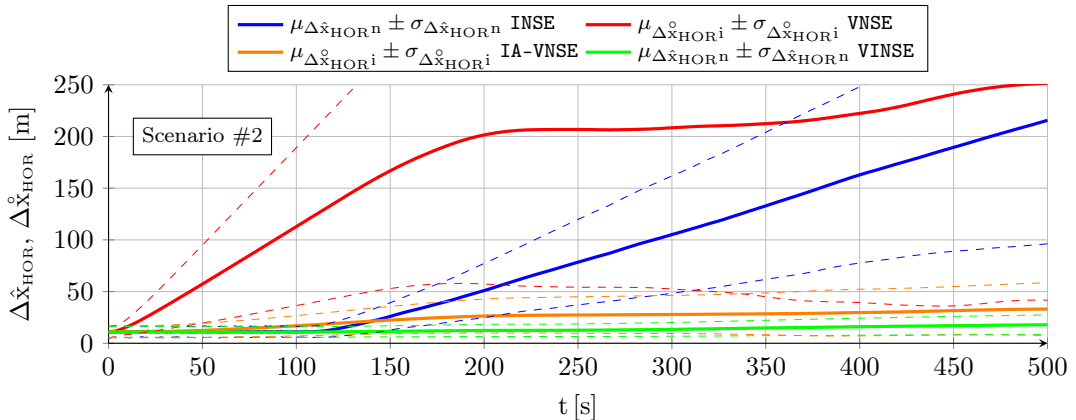


Figure 14: Horizontal position INSE, VNSE, IA-VNSE, and VINSE for scenario #2 (100 runs)

This two step reduction in the horizontal position error means that, although drift continues to be present due to the lack of absolute position observations in GNSS-Denied conditions, the horizontal position VINSEs are low enough so as to enable the autonomous aircraft to reach the vicinity of distant recovery locations in GNSS-Denied conditions, even when faced with turbulent and varying weather.

9 Summary of Results

This article proposes a VINS intended for fixed wing autonomous UAVs flying in GNSS-Denied conditions, which is composed by two algorithms (inertial and visual) that simultaneously control and assist each other. On one side, the IA-VNS presented in [6] complements a publicly available visual odometry pipeline such as SVO [7, 8] with priors based on the attitude and altitude VA-INS estimations so its visual estimations do not deviate in excess from its inertial counterparts. Its accurate incremental displacement outputs can be considered as the measurements of a virtual sensor (VVS) and employed by the VA-INS EKF as replacements for the GNSS receiver observations, as described in sections 5 and 6, resulting in major improvements when estimating the aircraft position without the use of GNSS signals. The results obtained when applying the proposed algorithms to high fidelity Monte Carlo simulations of two scenarios representative of the challenges of GNSS-Denied navigation indicate the following:

- The **VINS body attitude** estimation is qualitatively similar to that obtained by the standalone INS [5], which relies exclusively on an inertial filter without any visual algorithms. The bounded estimations (unbiased or zero mean for each Euler angle, biased for the total error as it is a norm) enable the aircraft to remain aloft in GNSS-Denied conditions for as long as it has fuel. Quantitatively, the VVS observations and the associated more accurate filter equations result in significant body attitude accuracy improvements in the two considered scenarios.
- The **VINS vertical position** estimation is qualitatively and quantitatively similar to that of the standalone INS [5] as both share the same algorithm, which freezes the atmospheric pressure offset estimation at the time that the GNSS signals are lost. In addition to ionospheric effects (which also apply when GNSS signals are available), the altitude error depends on the amount of pressure offset variation since entering GNSS-Denied conditions, being unbiased (zero mean), bounded by atmospheric physics, and valid for all navigation purposes except landing.
- The **VINS horizontal position** estimation exhibits drastic quantitative improvements over the baseline represented by the INS [5], which relies exclusively on an inertial filter without the use of onboard cameras and visual algorithms. Although from a qualitative point of view the estimation error is not bounded as the drift can not be fully eliminated, the horizontal position VINSE in the two evaluated scenarios is just a small fraction of the corresponding INSE. The reduced drift implies that the autonomous aircraft has a very high probability of at least reaching the vicinity of the predetermined recovery location, from where it can be landed by remote control, even if it requires flying for a long time in GNSS-Denied conditions while executing different types of maneuvers (turns, climbs or descents, airspeed changes) in the presence of turbulent and varying weather.

The improvement can be attributed to the two main fusion steps: using the accurate body attitude inertial estimations to limit the drift in the visual estimations [6], and simultaneously employing the ensuing more accurate horizontal position visual estimations to further reduce the inertial attitude errors (sections 5 and 6). The approach hence results in a virtuous loop in which both VINS components (IA-VNS and VA-INS) simultaneously assist and control each other.

10 Conclusions

The proposed visual inertial navigation filter, specifically designed for the challenges faced by autonomous fixed wing aircraft that encounter GNSS-Denied conditions, merges the observations provided by a suite of onboard sensors with those of the virtual vision sensor or VVS, resulting in major reductions in the horizontal position drift that increase the possibilities of the platform successfully reaching the vicinity of a recovery location from where it can be landed by remote control. The VVS is the denomination of the outputs generated by a visual inertial odometry pipeline that relies on the images of the Earth surface generated by an onboard camera as well as on the navigation filter outputs. The filter is implemented in the manifold of rigid body rotations or special

orthogonal group of \mathbb{R}^3 , known as $\mathbb{SO}(3)$, to minimize the accumulation of errors in the absence of the absolute position observations provided by the GNSS receiver.

A GNSS-Denied Navigation and Visual Inertial Odometry

The number, variety, and applications of Unmanned Air Vehicles (UAVs) have grown exponentially in the last few years, and the trend is expected to continue in the future [16, 17]. A comprehensive review of small UAV navigation systems and the problems they face is included in [18]. The use of Global Navigation Satellite Systems (GNSS) constitutes one of the main enablers for autonomous inertial navigation²² [19, 20, 21], but it is also one of its main weaknesses, as in the absence of GNSS signals inertial systems are forced to rely on dead reckoning, which results in position drift, with the aircraft slowly but steadily deviating from its intended route [22]. The availability of GNSS signals cannot be guaranteed; a throughout analysis of GNSS threats and reasons for signal degradation is presented in [23].

At this time there are no comprehensive solutions to the operation of autonomous UAVs in GNSS-Denied scenarios, for which the permanent loss of the GNSS signals is equivalent to losing the airframe in an uncontrolled way. A summary of the challenges of GNSS-Denied navigation and the research efforts intended to improve its performance are provided by [5, 24, 25]. Two promising techniques for completely eliminating the position drift are the use of *signals of opportunity*²³ [26, 27, 28], and *georegistration*²⁴ [29, 30, 31, 32], also known as *image registration*.

Visual Odometry (VO) consists on employing the ground images generated by one or more onboard cameras without the use of prerecorded image databases or any other sensors, incrementally estimating the vehicle pose (position plus attitude) based on the changes that its motion induces on the images [33, 34, 35, 36, 37]. It requires sufficient illumination, dominance of static scene, enough texture, and scene overlap between consecutive images or frames. Modern standalone algorithms such as Semi Direct Visual Odometry (SVO) [7, 8], Direct Sparse Odometry (DSO) [38], Large Scale Direct Simultaneous Localization and Mapping (LSD-SLAM) [39], and large scale feature based SLAM (ORB-SLAM)²⁵ [40, 41, 42] are robust and exhibit a limited drift. Although it has been employed for navigation of ground robots, road vehicles, and multirotors flying both indoors and outdoors, the incremental concatenation of relative poses results in a slow but unbounded pose drift that disqualifies VO for long term autonomous UAV GNSS-Denied navigation.

A promising research path to GNSS-Denied navigation appears to be the fusion of inertial and visual odometry algorithms into an integrated navigation system. Two different trends coexist in the literature, although an implementation of either group can sometimes employ a technique from the other:

- The first possibility, known as *filtering*, consists on employing the visual estimations as additional observations with which to feed the inertial filter. In the case of attitude estimation exclusively (momentarily neglecting the platform position), the GNSS signals are helpful and enable the INS to obtain more accurate and less noisy estimations, but they are not indispensable, as driftless attitude estimations can be obtained based on the IMU without their use. Proven techniques for attitude estimation in all kinds of platforms that do not rely on GNSS signals include Gaussian filters [43], deterministic filters [44], complimentary filters [45], and stochastic filters [46, 47]. In the case of the complete pose estimation (both attitude and position), it is indispensable to employ the velocity or incremental position observations obtained with VO methods in the absence of the absolute references provided by GNSS receivers. The literature includes cases based on Gaussian filters [48], and more recently nonlinear deterministic filters [49], stochastic filters [50], Riccati observers [51], and invariant extended Kalman filters or EKFs [52].

²²Inertial navigation is that which relies on the measurements provided by accelerometers and gyroscopes, also known as the Inertial Measurement Unit or IMU.

²³Existing signals originally intended for other purposes, such as those of television and cellular networks, can be employed to triangulate the aircraft position.

²⁴The position drift can be eliminated by matching landmarks or terrain features as viewed from the aircraft to preloaded data.

²⁵ORB stands for Oriented FAST and rotated BRIEF, a type of blob feature.

- The alternative is to employ VO optimizations with the assistance of the inertial navigation estimations, reducing the pose estimation drift inherent to VO. This is known as Visual Inertial Odometry (VIO) [53, 54], which can also be combined with image registration to fully eliminate the remaining pose drift. Current VIO implementations are also primarily intended for ground robots, multirotors, and road vehicles. VIO has matured significantly in the last few years, with detailed reviews available in [53, 54, 55, 56, 57].

There exist several open source VIO packages, such as the Multi State Constraint Kalman Filter (MSCKF) [58], the Open Keyframe Visual Inertial SLAM (OKVIS) [59, 60], the Robust Visual Inertial Odometry (ROVIO) [61], the monocular Visual Inertial Navigation System (VINS-Mono) [62], SVO combined with Multi Sensor Fusion (MSF) [7, 8, 63, 64], and SVO combined with Incremental Smoothing and Mapping (iSAM) [7, 8, 65, 66]. All these open source pipelines are compared in [53], and their results when applied to the EuRoC MAV data sets [13] are discussed in [14]. There also exist various other published VIO pipelines with implementations that are not publicly available [67, 68, 69, 70, 71, 72, 73], and there are also others that remain fully proprietary.

The existing VIO schemes to fuse the visual and inertial measurements can be broadly grouped into two paradigms: *loosely coupled* pipelines process the measurements separately, resulting in independent visual and inertial pose estimations, which are then fused to get the final estimate; on the other hand, *tightly coupled* methods compute the final pose estimation directly from the tracked image features and the IMU outputs [53, 54]. Tightly coupled approaches usually result in higher accuracy, as they use all the information available and take advantage of the IMU integration to predict the feature locations in the next frame. Loosely coupled methods, although less complex and more computationally efficient, lose information by decoupling the visual and inertial constraints, and are incapable of correcting the drift present in the visual estimator.

A different classification involves the number of images involved in each estimation [53, 54, 74], which is directly related with the resulting accuracy and computing demands. *Batch algorithms*, also known as *smoothers*, estimate multiple states simultaneously by solving a large nonlinear optimization problem or bundle adjustment, resulting in the highest possible accuracy. Valid techniques to limit the required computing resources include the reliance on a subset of the available frames (known as *keyframes*²⁶), the separation of tracking and mapping into different threads, and the development of incremental smoothing techniques based on factor graphs [66]. Although employing all available states (*full smoothing*) is sometimes feasible for very short trajectories, most pipelines rely on *sliding window* or *fixed lag smoothing*, in which the optimization relies exclusively on the measurements associated to the last few keyframes, discarding both the old keyframes as well as all other frames that have not been cataloged as keyframes. On the other hand, *filtering algorithms* restrict the estimation process to the latest state; they require less resources but suffer from permanently dropping all previous information and a much harder identification and removal of outliers, both of which lead to error accumulation or drift.

B Required Jacobians

This appendix groups together the various Jacobians employed in this article. They are the following:

- The time derivative of the geodetic coordinates $\mathbf{T}^{E,GDT} = [\lambda \phi h]^T$ (longitude, latitude, and altitude) depends on the NED velocity \mathbf{v}^N per (53), where M and N represent the WGS84 ellipsoid radii of curvature of meridian and prime vertical, respectively. The Jacobian with respect to \mathbf{v}^N , given by (54), is hence straightforward:

$$\dot{\mathbf{T}}^{E,GDT} = \begin{bmatrix} \frac{v_2^N}{[N(\varphi) + h] \cos \varphi} & \frac{v_1^N}{M(\varphi) + h} & -v_3^N \end{bmatrix}^T \quad (53)$$

$$\mathbf{J}_{\mathbf{v}^N} \dot{\mathbf{T}}^{E,GDT} = \begin{bmatrix} 0 & \frac{1}{(N+h) \cos \varphi} & 0 \\ \frac{1}{M+h} & 0 & 0 \\ 0 & 0 & -1 \end{bmatrix} \in \mathbb{R}^{3 \times 3} \quad (54)$$

²⁶Common criteria to identify keyframes involve thresholds on the time, position, or pose increments from the previous keyframe.

- The motion angular velocity $\omega_{\text{EN}} = \dot{\lambda} \mathbf{i}_3^E - \dot{\varphi} \mathbf{i}_2^N$ represents the rotation experienced by any object that moves without modifying its attitude with respect to the Earth surface. It is caused by the curvature of the Earth and its expression when viewed in NED is given by (55). Its Jacobian with respect to \mathbf{v}^N , provided by (56), is also straightforward:

$$\omega_{\text{EN}}^N = \begin{bmatrix} \frac{v_2^N}{N(\varphi) + h} & \frac{-v_1^N}{M(\varphi) + h} & \frac{-v_2^N \tan \varphi}{N(\varphi) + h} \end{bmatrix}^T \quad (55)$$

$$\mathbf{J}_{\mathbf{v}^N} \omega_{\text{EN}}^N = \begin{bmatrix} 0 & \frac{1}{N+h} & 0 \\ \frac{-1}{M+h} & 0 & 0 \\ 0 & \frac{-\tan \varphi}{N+h} & 0 \end{bmatrix} \in \mathbb{R}^{3 \times 3} \quad (56)$$

- The Coriolis acceleration $\mathbf{a}_{\text{cor}} = 2 \omega_{\text{IE}} \mathbf{v}$ is the double cross product between the Earth angular velocity caused by its rotation around the \mathbf{i}_3^E axis at a constant rate ω_E and the aircraft velocity. Its expression when viewed in NED is provided by (57), resulting in the (58) Jacobian with respect to \mathbf{v}^N :

$$\mathbf{a}_{\text{cor}}^N = 2 \hat{\omega}_{\text{IE}}^N \mathbf{v}^N = 2 \omega_E [v_2^N \sin \varphi \quad (-v_1^N \sin \varphi - v_3^N \cos \varphi) \quad v_2^N \cos \varphi]^T \quad (57)$$

$$\mathbf{J}_{\mathbf{v}^N} \mathbf{a}_{\text{cor}}^N = 2 \omega_E \begin{bmatrix} 0 & \sin \varphi & 0 \\ -\sin \varphi & 0 & -\cos \varphi \\ 0 & \cos \varphi & 0 \end{bmatrix} \in \mathbb{R}^{3 \times 3} \quad (58)$$

- The Lie Jacobian $\mathbf{J}_{\mathcal{R}}^{\mathcal{R} \oplus \Delta \mathbf{r}}$ represents the derivative of the function $f(\mathcal{R}, \Delta \mathbf{r}) = \mathcal{R} \oplus \Delta \mathbf{r}$, this is, the concatenation between the $\mathbb{SO}(3)$ attitude \mathcal{R} and its local perturbation $\Delta \mathbf{r}$, with respect to the $\mathbb{SO}(3)$ attitude \mathcal{R} , when the increments are viewed in their respective local tangent spaces, this is, tangent respectively at \mathcal{R} and $f(\mathcal{R}) = \mathcal{R} \oplus \Delta \mathbf{r}$. Interested readers should refer to [2, 4] for the obtainment of (59), where $\mathbf{R}(\Delta \mathbf{r})$ represents the direct cosine matrix corresponding to a given rotation vector $\Delta \mathbf{r}$, and the wide hat $\langle \hat{\cdot} \rangle$ refers to the skew-symmetric form of a vector:

$$\mathbf{J}_{\mathcal{R}}^{\mathcal{R} \oplus \Delta \mathbf{r}} = \mathbf{R}^T(\Delta \mathbf{r}) = \mathbf{R}(-\Delta \mathbf{r}) = \mathbf{I}_3 - \frac{\Delta \hat{\mathbf{r}}}{\|\Delta \mathbf{r}\|} \sin \|\Delta \mathbf{r}\| + \frac{(\Delta \hat{\mathbf{r}})^2}{\|\Delta \mathbf{r}\|^2} (1 - \cos \|\Delta \mathbf{r}\|) \in \mathbb{R}^{3 \times 3} \quad (59)$$

- The Lie Jacobian $\mathbf{J}_{\mathcal{R}}^{\mathbf{g}_{\mathcal{R}^*}(\mathbf{v})}$ represents the derivative of the function $f(\mathcal{R}, \mathbf{v}) = \mathbf{g}_{\mathcal{R}^*}(\mathbf{v})$, this is, the rotation of \mathbf{v} according to the $\mathbb{SO}(3)$ attitude \mathcal{R} , with respect to the $\mathbb{SO}(3)$ attitude \mathcal{R} , when the \mathcal{R} increment is viewed in its local tangent space and that of the resulting \mathbb{R}^3 vector is viewed in its Euclidean space. $\mathbf{J}_{\mathbf{v}}^{\mathbf{g}_{\mathcal{R}^*}(\mathbf{v})}$ is the derivative of the same function with respect to the \mathbb{R}^3 unrotated vector \mathbf{v} , in which the increments of the unrotated vector are also viewed in the \mathbb{R}^3 Euclidean space. Refer to [2, 4] for the obtainment of (60) and (61), where $\mathbf{R}(\mathcal{R})$ represents the direct cosine matrix corresponding to the rotation \mathcal{R} :

$$\mathbf{J}_{\mathcal{R}}^{\mathbf{g}_{\mathcal{R}^*}(\mathbf{v})} = -\mathbf{R}(\mathcal{R}) \hat{\mathbf{v}} \in \mathbb{R}^{3 \times 3} \quad (60)$$

$$\mathbf{J}_{\mathbf{v}}^{\mathbf{g}_{\mathcal{R}^*}(\mathbf{v})} = \mathbf{R}(\mathcal{R}) \in \mathbb{R}^{3 \times 3} \quad (61)$$

- The Lie Jacobians $\mathbf{J}_{\mathcal{R}}^{\mathbf{g}_{\mathcal{R}^*}^{-1}(\mathbf{v})}$ and $\mathbf{J}_{\mathbf{v}}^{\mathbf{g}_{\mathcal{R}^*}^{-1}(\mathbf{v})}$ are similar to the previous ones but refer to the inverse rotation action $f(\mathcal{R}, \mathbf{v}) = \mathbf{g}_{\mathcal{R}^*}^{-1}(\mathbf{v})$. Expressions (62) and (63) are also obtained in [2, 4], where the wedge symbol $\langle \cdot \wedge \cdot \rangle$ refers to the skew-symmetric form of a vector:

$$\mathbf{J}_{\mathcal{R}}^{\mathbf{g}_{\mathcal{R}^*}^{-1}(\mathbf{v})} = \left(\mathbf{R}^T(\mathcal{R}) \mathbf{v} \right) \wedge \in \mathbb{R}^{3 \times 3} \quad (62)$$

$$\mathbf{J}_{\mathbf{v}}^{\mathbf{g}_{\mathcal{R}^*}^{-1}(\mathbf{v})} = \mathbf{R}^T(\mathcal{R}) \in \mathbb{R}^{3 \times 3} \quad (63)$$

- The Lie Jacobian $\mathbf{J}_{\mathcal{R}}^{\text{Ad}_{\mathcal{R}}^{-1}(\omega)}$ represents the derivative of the function $f(\mathcal{R}, \omega) = \text{Ad}_{\mathcal{R}}^{-1}(\omega)$, this is, the inverse of the adjoint of ω according to the $\text{SO}(3)$ attitude \mathcal{R} , with respect to the $\text{SO}(3)$ attitude \mathcal{R} , when the \mathcal{R} increment is viewed in its local tangent space and that of the resulting \mathbb{R}^3 vector is viewed in its Euclidean space. $\mathbf{J}_{\omega}^{\text{Ad}_{\mathcal{R}}^{-1}(\omega)}$ is the derivative of the same function with respect to the \mathbb{R}^3 original vector ω . Refer to [2, 4] for the obtainment of (64) and (65):

$$\mathbf{J}_{\mathcal{R}}^{\text{Ad}_{\mathcal{R}}^{-1}(\omega)} = \left(\mathbf{R}^T(\mathcal{R}) \omega \right)^{\wedge} \in \mathbb{R}^{3 \times 3} \quad (64)$$

$$\mathbf{J}_{\omega}^{\text{Ad}_{\mathcal{R}}^{-1}(\omega)} = \mathbf{R}^T(\mathcal{R}) \in \mathbb{R}^{3 \times 3} \quad (65)$$

References

- [1] E. Gallo, “High Fidelity Flight Simulation for an Autonomous Low SWaP Fixed Wing UAV in GNSS-Denied Conditions.” https://github.com/edugallogithub/gnssdenied_flight_simulation, 2022. C++ open source code.
- [2] E. Gallo, “The SO(3) and SE(3) Lie Algebras of Rigid Body Rotations and Motions and their Application to Discrete Integration, Gradient Descent Optimization, and State Estimation,” 2022. [arXiv:2205.12572v1 \[cs.R0\]](https://arxiv.org/abs/2205.12572v1), <https://doi.org/10.48550/arXiv.2205.12572>.
- [3] J. Sola, “Quaternion Kinematics for the Error-State Kalman Filter,” 2017. [arXiv:1711.02508v1 \[cs.R0\]](https://arxiv.org/abs/1711.02508v1), <https://doi.org/10.48550/arXiv.1711.02508>.
- [4] J. Sola, J. Deray, and D. Atchuthan, “A Micro Lie Theory for State Estimation in Robotics,” 2018. [arXiv:1812.01537v9 \[cs.R0\]](https://arxiv.org/abs/1812.01537v9), <https://doi.org/10.48550/arXiv.1812.01537>.
- [5] E. Gallo and A. Barrientos, “Reduction of GNSS-Denied Inertial Navigation Errors for Fixed Wing Autonomous Unmanned Air Vehicles,” *Aerospace Science and Technology*, 2021. <https://doi.org/10.1016/j.ast.2021.107237>.
- [6] E. Gallo and A. Barrientos, “GNSS-Denied Semi Direct Visual Navigation for Autonomous UAVs Aided by PI-Inspired Priors,” *Aerospace*, 2023. <https://doi.org/10.3390/aerospace10030220>.
- [7] C. Forster, M. Pizzoli, and D. Scaramuzza, “SVO: Fast Semi-Direct Monocular Visual Odometry,” in *IEEE International Conference on Robotics and Automation*, 2014. <https://doi.org/10.1109/ICRA.2014.6906584>.
- [8] C. Forster, Z. Zhang, M. Gassner, M. Werlberger, and D. Scaramuzza, “SVO: Semidirect Visual Odometry for Monocular and Multicamera Systems,” *IEEE Transactions on Robotics*, 2016. <https://doi.org/10.1109/TRO.2016.2623335>.
- [9] E. Gallo and A. Barrientos, “Customizable Stochastic High Fidelity Model of the Sensors and Camera onboard a Fixed Wing Autonomous Aircraft,” *Sensors*, 2022. <https://doi.org/10.3390/s22155518>.
- [10] D. Simon, *Optimal State Estimation*. John Wiley & Sons, 2006. ISBN 0-471-70858-5.
- [11] J. L. Blanco, “A Tutorial on SE(3) Transformation Parameterizations and On-Manifold Optimization,” 2020. [arXiv:2103.15980v2 \[cs.R0\]](https://arxiv.org/abs/2103.15980v2), <https://doi.org/10.48550/arXiv.2103.15980>.
- [12] E. Gallo, “Stochastic High Fidelity Simulation and Scenarios for Testing of Fixed Wing Autonomous GNSS-Denied Navigation Algorithms,” 2021. [arXiv:2102.00883v3 \[cs.R0\]](https://arxiv.org/abs/2102.00883v3), <https://doi.org/10.48550/arXiv.2102.00883>.
- [13] M. Burri, J. Nikolic, P. Gohl, T. Schneider, J. Rehder, S. Omari, M. W. Achtelik, and R. Siegwart, “The EuRoC MAV Datasets,” *IEEE International Journal of Robotics Research*, 2016. <https://doi.org/10.1177/0278364915620033>.

[14] J. Delmerico and D. Scaramuzza, “A Benchmark Comparison of Monocular Visual-Inertial Odometry Algorithms for Flying Robots,” *IEEE International Conference on Robotics and Automation*, 2018. <https://doi.org/10.1109/ICRA.2018.8460664>.

[15] E. Gallo, “Quasi Static Atmospheric Model for Aircraft Trajectory Prediction and Flight Simulation,” 2021. [arXiv:2101.10744v1 \[eess.SY\]](https://arxiv.org/abs/2101.10744v1), <https://doi.org/10.48550/arXiv.2101.10744>.

[16] M. Hassanalian and A. Abdelkefi, “Classifications, Applications, and Design Challenges of Drones: A Review,” *Progress in Aerospace Sciences*, 2017. <https://doi.org/10.1016/j.paerosci.2017.04.003>.

[17] H. Shakhatreh, A. H. Sawalmeh, A. Al-Fuqaha, Z. Dou, E. Almaita, I. Khalil, N. S. Othman, A. Khreichah, and M. Guizani, “Unmanned Aerial Vehicles (UAVs): A Survey on Civil Applications and Key Research Challenges,” *IEEE Access*, 2019. <https://doi.org/10.1109/ACCESS.2019.2909530>.

[18] S. Bijaahalli, R. Sabatini, and A. Gardi, “Advances in Intelligent and Autonomous Navigation Systems for Small UAS,” *Progress in Aerospace Sciences*, 2020. <https://doi.org/10.1016/j.paerosci.2020.100617>.

[19] J. A. Farrell, *Aided Navigation, GPS with High Rate Sensors*. McGraw-Hill, Electronic Engineering Series, 2008.

[20] P. D. Groves, *Principles of GNSS, Inertial, and Multisensor Integrated Navigation Systems*. Artech House, GNSS Technology and Application Series, 2008.

[21] A. B. Chatfield, *Fundamentals of High Accuracy Inertial Navigation*. American Institute of Aeronautics and Astronautics, Progress in Astronautics and Aeronautics, vol 174, 1997.

[22] M. Elbanhawi, A. Mohamed, R. Clothier, J. Palmer, M. Simic, and S. Watkins, “Enabling Technologies for Autonomous MAV Operations,” *Progress in Aerospace Sciences*, 2017. <https://doi.org/10.1016/j.paerosci.2017.03.002>.

[23] R. Sabatini, T. Moore, and S. Ramasamy, “Global Navigation Satellite Systems Performance Analysis and Augmentation Strategies in Aviation,” *Progress in Aerospace Sciences*, 2017. <https://doi.org/10.1016/j.paerosci.2017.10.002>.

[24] C. Tippitt, A. Schultz, and W. Procino, “Vehicle Navigation: Autonomy Through GPS-Enabled and GPS-Denied Environments,” state of the art report DSIAC-2020-1328, Defense Systems Information Analysis Center, December 2020.

[25] N. Gyagenda, J. V. Hatilima, H. Roth, and V. Zhmud, “A Review of GNSS Independent UAV Navigation Techniques,” *Robotics and Autonomous Systems*, 2022. <https://doi.org/10.1016/j.robot.2022.104069>.

[26] R. Kapoor, S. Ramasamy, A. Gardi, and R. Sabatini, “UAV Navigation using Signals of Opportunity in Urban Environments: A Review,” *Energy Procedia*, 2017. <https://doi.org/10.1016/j.egypro.2017.03.156>.

[27] A. Coluccia, F. Ricciato, and G. Ricci, “Positioning Based on Signals of Opportunity,” *IEEE Communications Letters*, 2014. <https://doi.org/10.1109/LCOMM.2013.123013.132297>.

[28] S. T. Goh, O. Abdelkhalik, and S. A. Zekavat, “A Weighted Measurement Fusion Kalman Filter Implementation for UAV Navigation,” *Aerospace Science and Technology*, 2013. <https://doi.org/10.1016/j.ast.2012.11.012>.

[29] A. Couturier and M. A. Akhloufi, “A Review on Absolute Visual Localization for UAV,” *Robotics and Autonomous Systems*, 2020. <https://doi.org/10.1016/j.robot.2020.103666>.

[30] H. Goforth and S. Lucey, “GPS-Denied UAV Localization using Pre Existing Satellite Imagery,” in *IEEE International Conference on Robotics and Automation*, IEEE, 2019. <https://doi.org/10.1109/ICRA.2019.8793558>.

[31] N. Ziae, “Geolocation of an Aircraft using Image Registration Coupling Modes for Autonomous Navigation,” 2019. [arXiv:1909.02875v1 \[eess.IV\]](https://arxiv.org/abs/1909.02875v1), <https://doi.org/10.48550/arXiv.1909.02875>.

[32] T. Wang, “Augmented UAS Navigation in GPS Denied Terrain Environments using Synthetic Vision,” *Iowa State University Graduate Theses and Dissertations*, 15835, 2018. <https://doi.org/10.31274/etd-180810-5462>.

[33] D. Scaramuzza and F. Fraundorfer, “Visual Odometry Part 1: The First 30 Years and Fundamentals,” *IEEE Robotics & Automation Magazine*, 2011. <https://doi.org/10.1109/MRA.2011.943233>.

[34] F. Fraundorfer and D. Scaramuzza, “Visual Odometry Part 2: Matching, Robustness, Optimization, and Applications,” *IEEE Robotics & Automation Magazine*, 2012. <https://doi.org/10.1109/MRA.2012.2182810>.

[35] D. Scaramuzza, “Tutorial on Visual Odometry.” Robotics & Perception Group, University of Zurich, 2012. DOI not available.

[36] D. Scaramuzza, “Visual Odometry and SLAM: Past, Present, and the Robust Perception Age.” Robotics & Perception Group, University of Zurich, 2017. DOI not available.

[37] C. Cadena, L. Carlone, H. Carrillo, Y. Latif, D. Scaramuzza, J. Neira, I. Reid, and J. J. Leonard, “Past, Present, and Future of Simultaneous Localization and Mapping: Towards the Robust Perception Age,” *IEEE Transactions on Robotics*, 2016. <https://doi.org/10.1109/TRO.2016.2624754>.

[38] J. Engel, V. Koltun, and D. Cremers, “Direct Sparse Odometry,” *IEEE Transactions on Pattern Analysis and Machine Intelligence*, 2018. <https://doi.org/10.1109/TPAMI.2017.2658577>.

[39] J. Engel, T. Schops, and D. Cremers, “LSD-SLAM: Large Scale Direct Monocular SLAM,” *European Conference on Computer Vision*, 2014. https://doi.org/10.1007/978-3-319-10605-2_54.

[40] R. Mur-Artal, J. M. M. Montiel, and J. D. Tardos, “ORB-SLAM: a Versatile and Accurate Monocular SLAM System,” *IEEE Transactions on Robotics*, 2015. <https://doi.org/10.1109/TRO.2015.2463671>.

[41] R. Mur-Artal and J. D. Tardos, “ORB-SLAM2: an Open-Source SLAM System for Monocular, Stereo, and RGB-D Cameras,” *IEEE Transactions on Robotics*, 2017. <https://doi.org/10.1109/TRO.2017.2705103>.

[42] R. Mur-Artal, *Real-Time Accurate Visual SLAM with Place Recognition*. PhD thesis, University of Zaragoza, 2017. <https://doi.org/10.1109/TRO.2017.2705103>.

[43] J. L. Crassidis and F. L. Markley, “Unscented Filtering for Spacecraft Attitude Estimation,” *Journal of Guidance, Control, and Dynamics*, 2003. <https://doi.org/10.2514/2.5102>.

[44] H. F. Grip, T. I. Fossen, T. A. Johansen, and A. Saberi, “Attitude Estimation Using Biased Gyro and Vector Measurements with Time Varying Reference Vectors,” *IEEE Transactions on Automatic Control*, 2012. <https://doi.org/10.1109/TAC.2011.2173415>.

[45] R. Kottah, P. Narkhede, V. Kumar, V. Karar, and S. Poddar, “Multiple Model Adaptive Complementary Filter for Attitude Estimation,” *Aerospace Science and Technology*, 2017. <https://doi.org/10.1016/j.ast.2017.10.010>.

[46] H. A. Hashim, “Systematic Convergence of Nonlinear Stochastic Estimators on the Special Orthogonal Group SO(3),” *International Journal of Robust and Nonlinear Control*, 2020. <https://doi.org/10.1002/rnc.4971>.

[47] H. A. Hashim, L. J. Brown, and K. McIsaac, “Nonlinear Stochastic Attitude Filters on the Special Orthogonal Group SO(3): Ito and Stratonovich,” *IEEE Transactions on Systems, Man, and Cybernetics*, 2019. <https://doi.org/10.1109/TSMC.2018.2870290>.

[48] P. Batista, C. Silvestre, and P. Oliveira, “On the Observability of Linear Motion Quantities in Navigation Systems,” *Systems & Control Letters*, 2011. <https://doi.org/10.1016/j.sysconle.2010.11.002>.

[49] H. A. Hashim, L. J. Brown, and K. McIsaac, “Nonlinear Pose Filters on the Special Euclidean Group $SE(3)$ with Guaranteed Transient and Steady State Performance,” *IEEE Transactions on Systems, Man, and Cybernetics*, 2019. <https://doi.org/10.1109/TSMC.2019.2920114>.

[50] H. A. Hashim, “GPS Denied Navigation: Attitude, Position, Linear Velocity, and Gravity Estimation with Nonlinear Stochastic Observer,” *Proceedings of the 2021 American Control Conference*, 2021. <https://doi.org/10.23919/ACC50511.2021.9482995>.

[51] M.-D. Hua and G. Allibert, “Riccati Observer Design for Pose, Linear Velocity, and Gravity Direction Estimation Using Landmark Position and IMU Measurements,” *IEEE Conference on Control Technology and Applications*, 2018. <https://doi.org/10.1109/CCTA.2018.8511387>.

[52] A. Barrau and S. Bonnabel, “The Invariant Extended Kalman Filter as a Stable Observer,” *IEEE Transactions on Automatic Control*, 2017. <https://doi.org/10.1109/TAC.2016.2594085>.

[53] D. Scaramuzza and Z. Zhang, “Visual-Inertial Odometry of Aerial Robots,” 2019. [arXiv:1906.03289v2 \[cs.RO\]](https://arxiv.org/abs/1906.03289v2), <https://doi.org/10.48550/arXiv.1906.03289>.

[54] G. Huang, “Visual-Inertial Navigation: A Concise Review,” 2019. [arXiv:1906.02650v1 \[cs.RO\]](https://arxiv.org/abs/1906.02650v1), <https://doi.org/10.48550/arXiv.1906.02650>.

[55] L. von Stumberg, V. Usenko, and D. Cremers, “Chapter 7 - A Review and Quantitative Evaluation of Direct Visual Inertial Odometry,” in *Multimodal Scene Understanding* (M. Y. Yang, B. Rosenhahn, and V. Murino, eds.), Academic Press, 2019. <https://doi.org/10.1016/B978-0-12-817358-9.00013-5>.

[56] X. Feng, Y. Jiang, X. Yang, M. Du, and X. Li, “Computer Vision Algorithms and Hardware Implementations: A Survey,” *Integration, the VLSI Journal*, 2019. <https://doi.org/10.1016/j.vlsi.2019.07.005>.

[57] A. Al-Kaff, D. Martin, F. Garcia, A. de la Escalera, and J. Maria, “Survey of Computer Vision Algorithms and Applications for Unmanned Aerial Vehicles,” *Expert Systems With Applications*, 2017. <https://doi.org/10.1016/j.eswa.2017.09.033>.

[58] A. I. Mourikis and S. I. Roumeliotis, “A Multi-State Constraint Kalman Filter for Vision-aided Inertial Navigation,” *Proceedings 2007 IEEE International Conference on Robotics and Automation*, 2007. <https://doi.org/10.1109/ROBOT.2007.364024>.

[59] S. Leutenegger, P. Furgale, V. Rabaud, M. Chli, K. Konolige, and R. Siegwart, “Keyframe Based Visual Inertial SLAM Using Nonlinear Optimization,” *Robotics: Science and Systems*, 2013. <https://doi.org/10.3929/ethz-b-000236658>.

[60] S. Leutenegger, S. Lynen, M. Bosse, R. Siegwart, and P. Furgale, “Keyframe Based Visual Inertial SLAM Using Nonlinear Optimization,” *The International Journal of Robotics Research*, 2015. <https://doi.org/10.1177/0278364914554813>.

[61] M. Bloesch, S. Omari, M. Hutter, and R. Siegwart, “Robust Visual Inertial Odometry Using a Direct EKF Based Approach,” *International Conference of Intelligent Robot Systems*, 2015. <https://doi.org/10.3929/ethz-a-010566547>.

[62] T. Qin, P. Li, and S. Shen, “VINS-Mono: A Robust and Versatile Monocular Visual Inertial State Estimator,” *IEEE Transactions on Robotics*, 2018. <https://doi.org/10.1109/TRO.2018.2853729>.

[63] S. Lynen, M. W. Achtelik, S. Weiss, M. Chli, and R. Siegwart, “A Robust and Modular Multi Sensor Fusion Approach Applied to MAV Navigation,” *International Conference of Intelligent Robot Systems*, 2013. <https://doi.org/10.1109/IROS.2013.6696917>.

[64] M. Faessler, F. Fontana, C. Forster, E. Mueggler, M. Pizzoli, and D. Scaramuzza, “Autonomous, Vision Based Flight and Live Dense 3D Mapping with a Quadrotor Micro Aerial Vehicle,” *Journal of Field Robotics*, 2015. <https://doi.org/10.1002/rob.21581>.

- [65] C. Forster, L. Carlone, F. Dellaert, and D. Scaramuzza, “On Manifold Pre Integration for Real Time Visual Inertial Odometry,” *IEEE Transactions on Robotics*, 2017. <https://doi.org/10.1109/TRO.2016.2597321>.
- [66] M. Kaess, H. Johannsson, R. Roberts, V. Ila, J. Leonard, and F. Dellaert, “iSAM2: Incremental Smoothing and Mapping Using the Bayes Tree,” *The International Journal of Robotics Research*, 2012. <https://doi.org/10.1177/0278364911430419>.
- [67] R. Mur-Artal and J. M. M. Montiel, “Visual Inertial Monocular SLAM with Map Reuse,” *IEEE Robotics and Automation Letters*, 2017. <https://doi.org/10.1109/LRA.2017.2653359>.
- [68] R. Clark, S. Wang, H. Wen, A. Markham, and N. Trigoni, “VINet: Visual-Inertial Odometry as a Sequence-to-Sequence Learning Problem,” *Proceedings of the AAAI Conference on Artificial Intelligence*, 2017. <https://ojs.aaai.org/index.php/AAAI/article/view/11215>.
- [69] M. K. Paul, K. Wu, J. A. Hesch, E. D. Nerurkar, and S. I. Roumeliotis, “A Comparative Analysis of Tightly Coupled Monocular, Binocular, and Stereo VINS,” *IEEE International Conference on Robotics and Automation*, 2017. <https://doi.org/10.1109/ICRA.2017.7989022>.
- [70] Y. Song, S. Nuske, and S. Scherer, “A Multi Sensor Fusion MAV State Estimation from Long Range Stereo, IMU, GPS, and Barometric Sensors,” *Sensors*, 2017. <https://doi.org/10.3390/s17010011>.
- [71] A. Solin, S. Cortes, E. Rahtu, and J. Kannala, “PIVO: Probabilistic Inertial Visual Odometry for Occlusion Robust Navigation,” *IEEE Winter Conference on Applications of Computer Vision*, 2018. <https://doi.org/10.1109/WACV.2018.00073>.
- [72] S. Houben, J. Quenzel, N. Krombach, and S. Behnke, “Efficient Multi Camera Visual Inertial SLAM for Micro Aerial Vehicles,” *IEEE/RSJ International Conference on Intelligent Robots and Systems*, 2016. <https://doi.org/10.1109/IROS.2016.7759261>.
- [73] K. Eckenhoff, P. Geneva, and G. Huang, “Direct Visual Inertial Navigation with Analytical Preintegration,” *IEEE International Conference on Robotics and Automation*, 2017. <https://doi.org/10.1109/ICRA.2017.7989171>.
- [74] H. Strasdat, J. M. M. Montiel, and A. J. Davison, “Real Time Monocular SLAM: Why Filter?,” *IEEE International Conference on Robotics and Automation*, 2010. <https://doi.org/10.1109/ROBOT.2010.5509636>.